Investigation of Resonant Inter Coulombic Decay and Radiative Charge Tranfer in Rare Gas Cluster after Inner-Shell Excitation using Fluorescence Spectroscopy and Photon-Electron-Coincidence Experiments

Universität Kassel

Johannes Heinrich Viehmann

August 17, 2021

Abstract

Within this thesis two different ways of integrating fluorescence spectroscopy into the search for interatomic processes after resonant excitation of neon-krypton clusters are presented.
Evidence for radiative charge transfer is shown in fluorescence data proposing an electron-photon correlation manifesting itself in the fluorescence signal.
The advantages of coincident particle measurements for enhancing resonant interatomic coulomb decay signals are illustrated and discussed using electron-photon coincidence data from neon-krypton clusters.

Declaration

I warrant that the thesis is my original work and that I have not received outside assistance. Only the sources cited have been used in this draft. Parts that are direct quotes or paraphrases are identified as such.

Ort, Datum

Unterschrift

Contents

Chapter 1

Introduction

The scope of this thesis is (in more general terms) to provide an overview of fundamental questions about processes in certain quantum mechanical systems and experimental techniques to study these. More specifically, the quantum systems of interest in this thesis are conglomerates of particles called *cluster*.
Investigations of different quantum systems have been performed and are still pursued in current experiments by several research communities. A prominent example of this is the atom and molecular physics community trying to discover and describe phenomena in quantum systems consisting of single atoms or molecules. Only very recently have researchers started to look into the processes within atomic or molecular cluster systems. Since clusters act as a bridge between single particles and complex systems, it is indispensable for a deeper understanding to further investigate these conglomerates of particles.
So far, we are able to solve the equations associated with just few interacting particles analytically. For the behaviour of many interacting particles, approximations and numerical approaches have to be used. The existing models are very accurate for certain many-particle-systems, as solid state physics demonstrates, but a more complete understanding of the transition from few particle behaviour to a complex system of interacting particles is needed. Additionally, the complex interplay of particles is a phenomena frequently observed in nature.
The question arises, if the interplay of multiple particles does open up new interaction possibilities or decay channels for the particles. And, indeed, around 25 years ago Lorentz Cederbaum performed the following *Gedanken-*

experiment: He calculated new electronic decay channels for atoms bound by weak interacting forces to other atoms. Cederbaum predicted that an energetic excitation in one atom of the cluster could be transferred to a neighbouring atom and used to ionize this neighbour (the decay channel was named Interatomic Coulomb Decay or ICD). The predictions could be confirmed experimentally less than 10 years later using charged particle spectroscopy, a traditional tool of atom and molecular physics.

Within this field of research and the different cluster systems imaginable, this thesis will focus on rare gas cluster, which consist of rare gas atoms bound together by van-der-Waals forces. The binding potentials of such interactions are small compared to thermal energies of particles under normal conditions. Although this means that rare gas clusters are not common in nature, they provide a good laboratory environment for simulating dense media such as is found in biological tissue. Furthermore, using rare gas atoms is convenient due to their *simplicity* in terms of mathematical description and experimental handling.
The experimental methods used in this work are focusing on fluorescence spectroscopy. The group around Professor Arno Ehresmann (AGE) from the Universität Kassel were the first to measure evidence of ICD like processes in fluorescence spectra of clusters, thereby establishing a new experimental detection method within the atomic and molecular cluster community. This thesis will deal with some distinct advantages and disadvantage of detecting fluorescence signals from cluster systems.

At first, the goal of this work is to give a brief overview of fluorescence spectroscopy applied to the search for cluster-specific electronic decay mechanisms. For this, an exemplary analysis of two fluorescence experiments conducted on homogeneous neon-neon and heterogeneous neon-krypton cluster is presented. In order to paint a full picture, the following chapter will concentrate on theoretical background of atomic physics and cluster-specific processes, as well as explain the basic experimental techniques of fluorescence and coincidence spectroscopy.
The analytical part of the thesis stresses the difference of properties of atomic and interatomic processes and the usefulness of establishing a variety of well studied detection methods.

Chapter 2

Background

This chapter will deal with the theoretical and experimental basics that are needed to follow the process of data acquisition and analysis. In order to gain an understanding of the implications of intermolecular electronic processes, one first has to consider the underlying concepts of quantum mechanics.

2.1 Fundamental Physical Background

There have been numerous books and lectures on quantum mechanics, which this chapter will try to shortly summarize. The literature is pointed out for deeper mathematical background [1][2].

Quantum Mechanics and Atoms

For the last century, physicists used the formalisms of quantum mechanics in order to describe electronic processes in atoms and molecules. This includes finding the properties of the particle in its energetic ground state, as well, as investigating decay mechanisms after these have been promoted into excited states.
One important mathematical tool underlying the description of quantum mechanics is given by the Schrödinger equation

$$\hat{H} \left|\Psi(t)\right\rangle = i\hbar \frac{\partial}{\partial t} \left|\Psi(t)\right\rangle \ , \tag{2.1}$$

introducing the Hamilton operator $\hat{H}$, the state vector $|\Psi\rangle$, the imaginary unit i and the reduced Planck constant $\hbar$.

The Schrödinger equation is a differential equation describing the evolution of the state vector $|\Psi\rangle$ over time, where this vector is defined in a Hilbert space and characterizes the quantum mechanical system.
The Hamilton operator (or Hamiltonian) describes a quantum system's total energy. Its eigenvalues are all the possibly measurable energies. Solving the Schrödinger equation for small (hydrogen-like) atoms is analytically possible. For this, one assumes a stationary system, which breaks equation (2.1) down to

$$\hat{H}\,|\Psi\rangle = E\,|\Psi\rangle\ . \tag{2.2}$$

This time-independent (or stationary) Schrödinger equation is an eigenvalue equation, with the energy E being the eigenvalues of the Hamiltonian $\hat{H}$ and the state vectors $|\Psi\rangle$ being the eigenfunctions of $\hat{H}$.
For the simplest case, a hydrogen atom, the Hamiltonian can be described as the sum of the kinetic energy of the electron $\hat{T}$ and the potential energy landscape $\hat{V}$ formed by the Coulomb force of the nucleus acting upon the electron

$$\hat{H} = \hat{T} + \hat{V} = \frac{\hat{p}^2}{2\mu} + \frac{e^2}{4\pi\epsilon_0|\vec{r}|}\ . \tag{2.3}$$

With the momentum operator $\hat{p} = -i\hbar\nabla$ and the reduced mass μ of the system. Also using the natural constants of the elementary charge e, the vacuum permittivity $epsilon_0$ and π. The whole equation depends on the relative position $\vec{r}$ between the nucleus and the electron.
Solving equation (2.2) with the Hamiltonian (2.3) is done using spherical coordinates, which makes handling the spherical symmetry of the potential easier. By doing so the components of $\hat{T}$ and $\hat{V}$ in the spherical representation can be separated into one part only depending on the distance r and one part only depending on the angles θ and φ. These two parts are solved by the radial function $R_{nl}(r)$ and the spherical harmonics $Y_{lm}(\varphi,\theta)$ respectively [2]. These separated functions together form the total wave function $\Psi_{nlm}(r,\varphi,\theta)$ of an electron in the potential of a hydrogen nucleus

$$\Psi_{nlm}(r,\varphi,\theta) = R_{nl}(r)Y_{lm}(\varphi,\theta)\,. \tag{2.4}$$

$R_{nl}(r)$ and $Y_{lm}(\varphi,\theta)$ introduce three numbers, n, l and m, which will turn out to be useful for a description of electronic energy states for atoms, the quantum numbers.
n is the principle quantum number, which puts the different energy states of

an electron within an atom into perspective depending on the mean distance of the electron from the nucleus. Electrons having the same quantum number n are said to occupy the same electron shell of the atom. The quantum number l is called the azimuthal (or orbital angular momentum) quantum number. It corresponds to a classical view of an electron possessing an angular momentum on its way around the nucleus and determines the shape of the electron's atomic orbital. The magnetic quantum number m further defines the orientation of the angular momentum l. The spin quantum number s is omitted at this point for simplicity reasons.
The quantum numbers are restricted to the values

$$n \in \mathbb{N}_{/0} \tag{2.5}$$

$$l = \underbrace{0, 1, 2}_{s,p,d,...}, ..., n-1 \tag{2.6}$$

$$m = -l, -l+1, ..., 0, ..., l-1, l\,, \tag{2.7}$$

which directly displays an important aspect of quantum mechanics, its quantization. It can be seen by solving the stationary Schrödinger equation (2.2) using the Hamiltonian (2.3) and the found wave function (2.4)

$$\langle \Psi_{nlm} | \, \hat{H} \, | \Psi_{nlm} \rangle = E_{nlm}\,, \tag{2.8}$$

that the energies E_{nlm} of a considered quantum system, will depend on the quantum numbers and only be able to take on discrete energy values.
Figure 2.1 schematically shows the electronic configuration of a neon atom. The concept of quantized energy levels is visualized using horizontal lines on which the gray balls represent the electrons. The quantum numbers n and l of each level are noted to the left of the respective horizontal line. The letters represent the angular momentum quantum number l as mentioned in the under brace of equation (2.6). The multiple lines denoted with np are sketching unoccupied orbitals that are still bound to the atom. These are, in the case of the later data analysis, p orbitals of principle quantum number $n > 2$ (other orbitals of quantum number $l \neq 1$ are omitted for simplicity reasons). The energies to the right of the shells accounts for its binding energy. This is the energy incoming radiation needs to introduce to an electron from the respective shell in order to lift it into the vacuum state. The vacuum state is shown in the figure above the thick black line at the

top. An electron above this threshold is a free particle. Here, the nucleus potential is essentially zero and the electron is not effected by it any more.

Equation (2.8) essantially states that electrons that are bound to nuclei will

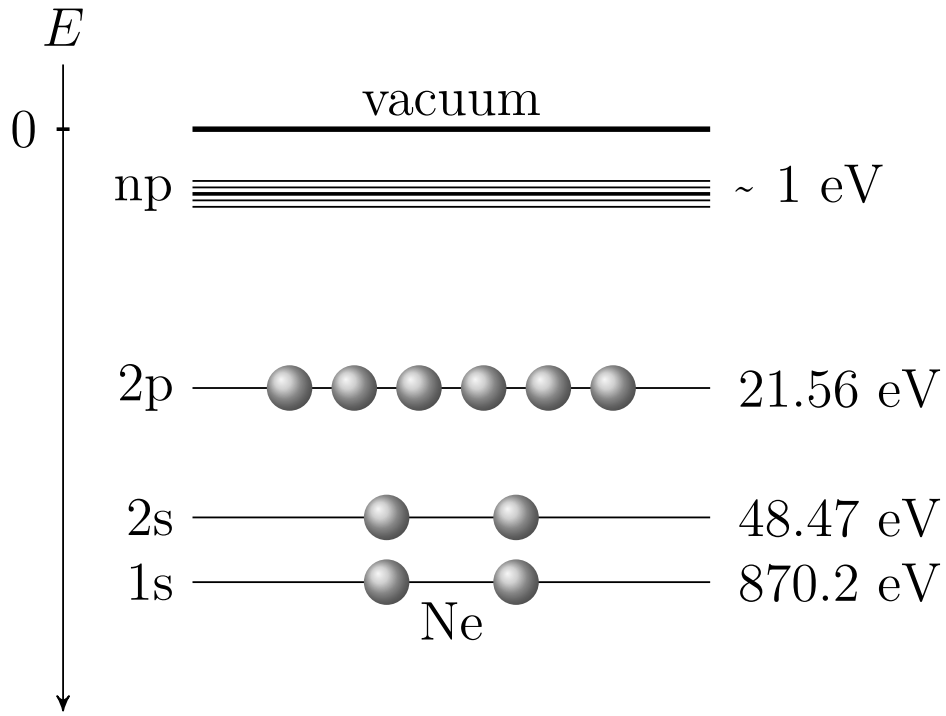

Figure 2.1: Scheme of the electronic configuration of a neon atom. The gray balls represent the electrons of the atom occupying different shells corresponding to the energy levels E_n that were described by the solution of the Schrödinger equation (2.8). The different orbitals are shown by the horizontal lines and named by the number and letter to the left of the line. The number is the value of the principle quantum n, while the letter represents the azimuthal quantum number l (s: $l = 0$, p: $l = 1$). The multiple lines denoted with np are showing the closely lying Rydberg states of neon with $n \in \mathbb{N}_{>2}$. To the right of the horizontal lines there are the binding energies of each orbital. Above the thick black line at the top lies the vacuum state for the electrons, where the potential of the atom's nucleus is essentially zero.

occupy certain discrete energy levels E_{nlm}. In the scheme of figure 2.1 this means that electrons do not occupy any space in between the lines. Further, the configuration shown in this picture is the electronic configuration with

the lowest total energy of the system, the energetic ground state. or simply ground state This means especially, that no electronic transitions into lower lying states are possible due to another interesting phenomena of quantum mechanics, the Pauli's exclusion principle. It states that no two fermions (particles with half-numbered spin, e.g. electrons with $s = \pm\frac{1}{2}$) can posses the exact same set of quantum numbers.
The reason figure 2.1 shows multiple electrons on the same energy line is the omitted quantum numbers m and s. In the scheme only n and l were taken into consideration. All the electrons with same n and l quantum number posses the same energy in this schemeand are hence described as energetically degenerate regarding m and s. Therefore, six electrons occupy the $2p$ orbital, since p corresponds to $l = 1$, which means the magnetic quantum number takes on the values $m = -1, 0, 1$ and each m creating an own subshells. Further, each subshell can contain electrons of two different spins $s = \pm\frac{1}{2}$. For the s shells (s meaning $l = 0$) equation (2.7) results in only one m subshellsn again filled by two electrons with different spin quantum numbers s.

Light-Matter Interaction: Theory

Light-matter interaction refers to the interaction between electromagnetic waves and the fundamental building blocks of matter, i.e. atoms or molecules. Figure 2.1 shows the energy landscape of a stationary neon atom. But how does it change when energy is introduced into the system? For such an investigation the concepts of light-matter interaction are of high importance [3].
The most commonly used tool for investigating light-matter interaction experimentally is spectroscopy, the interrogation of matter with light. This method cannot "see" the atom or molecule itself, but rather the influence it has on the light. By detecting the light after the interaction and comparing it to theoretical models, it is possible to make statements about the electronic processes happening (other excitation regimes not shown in this work can also resolve molecular vibration or rotational levels). This means, both spectroscopy and theoretical framework go hand in hand and are dependent on each other.
Light-matter interaction can be modelled mathematically using a semi-classical picture (for a full quantum mechanical picture one has to introduce the concepts of quantum electrodynamics QED [4]). However, the principle ideas

are the same in both semi-classical and QED model. The Hamiltonian $\hat{H}$ describing an atomic system interacting with light can be separated into time dependent and independent parts

$$\hat{H} = \hat{H}_0 + \hat{H}'(t)\,. \tag{2.9}$$

The stationary Hamiltonian $\hat{H}_0$ describes the atom or molecule with no light interaction as it was discussed in the previous section. This part has no time dependence and is formulated in the quantum mechanical picture. The time-dependent part $\hat{H}'(t)$ can be viewed as a perturbation acting on the stationary atom or molecule.
To define the perturbation more closely in a semi-classical description of electromagnetic waves interacting with charges, the vector potential $\hat{A}(\vec{r},t)$ and the scalar potential ϕ of the electromagnetic field are used. $\hat{A}(\vec{r},t)$ is needed in order to describe the time evolution of the electromagnetic field propagation in space and time. ϕ can be neglected by choosing the Coulomb gauge and arguing that the contribution of the scalar potential compared to the nucleus potential included in the stationary Hamiltonian $\hat{H}_0$ is small. Therefore, the perturbation part $\hat{H}'(t)$ of the Hamiltonian $\hat{H}$ can be written as

$$\hat{H}'(t) = \sum_{j=1}^{N} \frac{q_j}{m_j}\hat{A}\cdot\hat{p}_j + \frac{q_j^2}{2m_j}\hat{A}^2\,. \tag{2.10}$$

Summing here over all charged particles j with mass m_j and charge q_j interacting with the field of the radiation (first part of the sum). The second part of the sum, which is proportional to the square of the vector potential, can be dropped, since perturbation theory only considers small perturbations to the stationary system. Therefore, this ansatz will hold only for low intensities of the incoming electromagnetic wave, which eventually makes the squared part of the sum small compared to the nucleus potential. Generally, one has to consider this part only for high light intensities $I > 10^{15}\,\mathrm{W/cm^2}$, e.g. strong laser light.
Using $\hat{A} = \vec{A}_0 e^{-i\vec{k}\vec{r}}$ the Hamiltonian $\hat{H}'_{\mathrm{hydrogen}}(t)$ for a hydrogen atom can be obtained [5]

$$\hat{H}'_{\mathrm{hydrogen}}(t) = \vec{A}_0 e^{-i\vec{k}\vec{r}}\frac{e}{m_e}\hat{p}\,. \tag{2.11}$$

$\vec{A}_0$ carries the information about the amplitude and polarisation of the electromagnetic wave and $\vec{k}$ is the wave vector.
When the wavelength of the electromagnetic wave is big compared to the atomic radius, it is a fair assumption to expand the exponential function

$$e^{-i\vec{k}\vec{r}} = \sum_{n=0}^{\infty} \frac{(i\vec{k}\vec{r})^n}{n!} \tag{2.12}$$

and consider only the first order ($n = 0$), which will contribute to the Hamiltonian with a factor 1. This approximation is called the dipole approximation.
The experiments examined in the following chapters involve X-ray excitation energies of the order of $10^1\,\mathrm{eV}$, which translates into a wavelength of the order of $\lambda \approx 10^1\,\mathrm{nm}$. Thus, the approximation is useful in the presented case, nevertheless, higher order multipole moments have to be considered, generally.
Taking the dipole approximation into account (2.11) becomes

$$\hat{H}'_{\mathrm{hydrogen}}(t) = \vec{A}_0 \frac{e}{m_e} \hat{p}\,. \tag{2.13}$$

Finally, it is known from perturbation theory that the transition probability W_{fi} between an initial state $|i\rangle$ and a final state $|f\rangle$ depends only on the perturbation part of the Hamiltonian $\hat{H}'$. This, again, is a series expansion from which only the first order is considered

$$W_{fi} = \frac{2\pi}{\hbar} |\hat{H}'_{fi,\mathrm{hydrogen}}|^2 \; \delta(E_f - E_i - \hbar\omega)\,. \tag{2.14}$$

δ is Dirac's delta-function, which contains the energy of the final E_f and initial E_i state and the energy of the incoming radiation $\hbar\omega$. The matrix element $\hat{H}'_{fi,\mathrm{hydrogen}}$ can be further simplified by switching into the Heisenberg representation and replacing $\hat{p}$ by the respective presentation of the position operator $\hat{r}$

$$\begin{aligned}
\hat{H}'_{fi,\mathrm{hydrogen}} &= \langle f|\, \hat{H}'_{\mathrm{hydrogen}}\, |i\rangle && (2.15)\\
&= \vec{A}_0 \frac{e}{m_e} \langle f|\, \hat{p}\, |i\rangle \propto e\, \langle f|\, \hat{r}\, |i\rangle && (2.16)\\
&\propto \langle f|\, e\hat{r}\, |i\rangle = \langle f|\, \hat{D}\, |i\rangle && (2.17)\\
\Rightarrow W_{fi} &\propto |\, \langle f|\, \hat{D}\, |i\rangle\, |^2 = |\hat{D}_{fi}|^2\,. && (2.18)
\end{aligned}$$

The operator $\hat{D} = e \cdot \hat{r}$ is the dipole operator, representing the light-matter interaction $\hat{H}'$ in this perturbation theoretical ansatz using the described approximations and $\hat{D}_{fi}$ are the dipole transition matrix elements, explicitly for the transition between initial state $|i\rangle$ and final state $|f\rangle$.
Fermi's golden r=ule described by equation (2.14) and its dependency on the dipole transition moment $\hat{D}_{fi}$ ((2.18) is suited to tackle the questions of light absorption and emission by matter. Also, the dipole transition moments $\hat{D}_{fi}$ can be zero between two states, which means a transition is not possible, when only considering a dipole interaction between the incoming radiation and the atom or molecule. In such a case, one speaks of dipole forbidden transitions. These transitions might still be observable, but for their calculation a higher order within the multipole expansion in (2.12) or Fermi's golden rule (2.14) need to be considered.
The next sections will apply the consequences of light-matter interaction to the example of neon (figure 2.1).

Light-Matter Interaction: Experiment

In order to do proper experimental analysis an expectation about the experimental outcome should be considered. Using the mathematical formulations of the previous section there are some predictions that can be made.
Firstly, Fermi's golden rule from equation (2.14) directly relates incoming photon energy $\hbar\omega$ and the energy states of the interacting atomic or molecular system E_f and E_i. These terms are all connected within Dirac's delta-function. This implies that the energies obey

$$\delta(E_f - E_i - \hbar\omega) = \begin{cases} 1 & , if \quad E_i + \hbar\omega = E_f \\ 0 & , if \quad E_i + \hbar\omega \neq E_f \end{cases} \quad . \tag{2.19}$$

This basically describes energy conservation, but is kind of interesting for a quantum system. So, the transition probability W_{fi} only exists, if the sum of the incoming radiation energy and the energy of the initial state match the energy of the final state. Applying this to the scheme of the neon atom from figure 2.1, there are two different cases to be distinguished: the incoming photon has enough energy to promote an electron above the vacuum threshold ($\hbar\omega > I_p$: lowest ionization potential) or it doesn't ($\hbar\omega < I_p$).
For the first case, it is simple. The energy of the final state is the solution of the Schrödinger equation for a free particle, which can be described by

plane waves and can posses a continuum of energies. Therefore, the vacuum is called the continuum state of electrons and the process of promoting an electron into the continuum is called ionization. The atom left behind by the ionized electron carries a net charge of $q = -e$ and is called an ion. The free electron is called photoelectron and has a kinetic energy $E_{kin} = E_b - \hbar\omega$, which is related to the binding energy E_b of the electron and the energy of the incoming photon $\hbar\omega$. Since the binding energy is an intrinsic property of the element that is investigated, the photoelectrons kinetic energy scales proportionally with the energy of the ionizing radiation

$$E_{kin} \propto \hbar\omega \,. \tag{2.20}$$

The transition probability W_{fi} for an ionization process will have a certain value greater zero, because the respective condition for the δ-function in equation (2.19) can always be met in a continuum state, where all possible realizations of E_f are feasible.
The second case, $\hbar\omega < I_p$, does not provide a continuum of final states E_f, since the energy of the states within the atom is quantized as discussed in the earlier sections. If the incoming photon energy $\hbar\omega$ is not exactly matching the energy difference between two states $|i\rangle$ and $|f\rangle$ (off-resonant), Dirac's delta-function (2.19) will yield zero and thus the transition probability W_{fi}. Only if the energy matches exactly, there will be a so-called resonant excitation from one bound electronic state to another. The frequency of photons matching these resonance condition is called resonance frequency ω_r.
At this point, it is worth mentioning that the most widely used experimental method of finding these transition probabilities W_{fi} is spectroscopy. Here, the measured intensities I of interaction products (e.g. emitted photoelectrons) are directly proportional to the transition probabilities calculated by Fermi's golden rule. The delta-function included in the calculation will, nevertheless, rather be a Lorentz profile with a non-vanishing width due to the uncertainty correlation between the energy ΔE and the life time of the initial state Δt, which states $\Delta E \Delta t \leq \hbar$. This means that short living states, will decay with a not clearly defined energy and therefore the resonance condition is not strictly obeyed. Other phenomena like the pressure of the medium surrounding atoms or the velocity the atom carries, can further broaden the emission or absorption features of atoms and molecules.

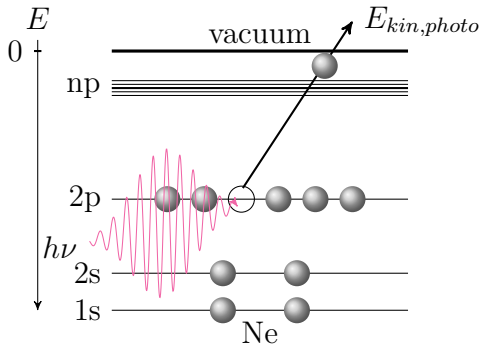

(a) Ionization

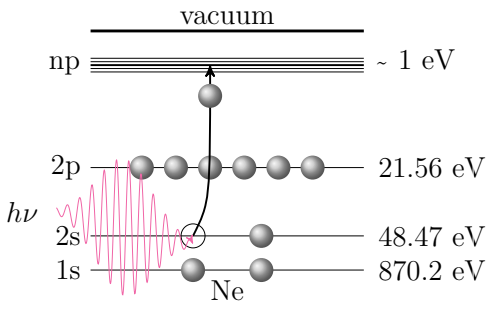

(b) Resonant excitation

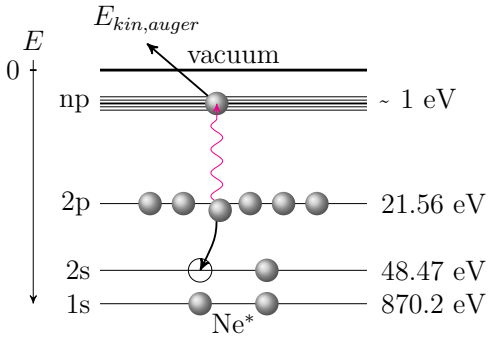

(c) Autoionization

Figure 2.2: Scheme showing electronic processes after light-matter interaction with a photon of energy $\hbar\omega$. (a) shows the direct photo ionization of a $2p$ electron. (b) depicts a resonant excitation from a $2s$ electron into a np orbital ($n = 3, 4, 5, \ldots$). If $\hbar\omega > I_{2p}$ both processes will take place. (c) shows an Auger decay for the neon atom. The initially excited electron in the np state is ionized by the excess energy from the transition of one $2p$ electron into the $2s$ hole.

Figure 2.2 shows the examples of neon undergoing resonant excitation and ionization processes. An example with incident radiation energies above the lowest ionization potential $I_p = I_{p,2p} = 21.56\,\text{eV}$ was chosen. This will illustrate, even though the energy is high enough to ionize an atom directly,

resonant excitation processes can and will compete with the ionization process and both will happen corresponding to their probability W_{fi}.
In figure 2.2a the ionization process is shown. An incoming photon shown by the magenta wave package and denoted with the energy term $\hbar\omega$ is transferring its energy to a $2p$ electron. With $\hbar\omega > I_{p,2p}$ the electron will be freed from the atomic potential and carry the kinetic energy $E_{kin,photo} = \hbar\omega - I_{p,2p}$. An experimentalist measuring the electrons coming out of this light-matter interaction should expect no electrons unless the exciting-photon energy $\hbar\omega$ exceeds the ionization potential $I_{p,2p}$, because the $2p$ electron is the weakest bound electron of neon. Photons carrying less energy ($\hbar\omega < I_{p,2p}$) are not sufficient to produce free electrons. In this case, $I_{p,2p}$ corresponds to the absorption edge of neon, beneath which the atoms cannot be ionized. In other words, the probability of ionization below $I_{p,2p}$ is essentially zero, but increases strongly for light energies just above the edge. For higher photon energies the interaction probability will form a sort of a plateau, which will become slightly more transparent for very high photon energies again. If the experimentalist decides to measure the photoelectrons' energies depending on the excitation energy of the photons, the result would be expected to show a linear correlation between both. The higher the incoming photon energies, the faster the created photoelectron corresponding to equation (2.20).
Figure 2.2b depicts the resonant excitation from the $2s$ orbital to a np state. If the resonance frequency $\omega_r = E_{2s} - E_{np}$ is matched by the incoming lights energy, the transition from a $2s$ electron into a np shell is possible. One can see from the binding energies noted in the figure, that the resonance frequency between these states will roughly be

$$\hbar\omega_r = \frac{E_r}{\hbar} = \frac{E_{2s} - E_{np}}{\hbar} \approx 47\,\mathrm{eV}/\hbar\,, \tag{2.21}$$

with E_r being the energy of the photon carrying the resonance frequency ω_r. Looking at the binding energy of the $2p$ electron and the excitation energy of a $2s - np$-resonant photon ($E_{2p} = 21.56\,\mathrm{eV} < E_r \approx 47\,\mathrm{eV}$) it is evident that both processes are energetically possible. And since they are both quantum mechanically allowed, they will compete.
After the resonant excitation, though, the atom is not in the ground state, yet. A relaxation will occur. In general, this relaxation will happen by emitting a photon (fluorescence) or by exciting another electron into the continuum (autoionization).
Figure 2.2c displays the latter effect in the form of an Auger decay. The

initially created hole in the $2s$ shell is filled by a $2p$ electron. The excess energy being released by this transition is transported to the excited electron in the np shell, which is than ionized. The free electron is often referred to as Auger electron and has a kinetic energy $E_{kin,Auger} = E_{2s} - E_{2p} - E_{np}$ only depending on the binding energies of the orbitals involved in the transitions. This implies, the Auger electron will not be measured with a continuous energy spectrum, but rather with certain discrete energies defined by the atomic environment.
There is a notation for electronic configurations of atoms and molecules, which can describe the processes mentioned above very precisely [2]. The formulation uses the quantum numbers n and l to describe the amount of electrons n_e in each nl-subshell using the formulation

$$nl^{n_e} .$$

In order to describe the configuration of all electrons belonging to an atom all occupied orbitals are written down from energetically strongest to weakest bound orbital. A neon atom in the ground state would, therefore, correspond to

$$1s^2 2s^2 2p^6 .$$

Electronic processes or light-matter interaction can also be described in this way. The photo ionization or Auger decay shown in figure 2.2 can be written as

$$1s^2 2s^2 2p^6 + \hbar\omega \rightarrow 1s^2 2s^2 2p^5 \epsilon l$$

for the photo ionization and

$$1s^2 2s^2 2p^6 + \hbar\omega \rightarrow 1s^2 2s^1 2p^6 np^1 \rightarrow 1s^2 2s^2 2p^5 \epsilon l$$

for the Auger decay. The part ϵl denotes for the outgoing electron wave of the emitted electron and depends on the quantum number l. Remarkable is the fact, that both final states have the same electron configuration, but undergo different paths. The Auger decay involving the unstable intermediate states, e.g. $1s^2 2s^1 2p^6 3p^1$ (schematically shown in figure 2.2b), which consecutively decay into the final state.
The notation explained above is often found abbreviated in the literature. States that are not taking part in interactions or electron transitions are

omitted and instead of noting the total amount of electrons in an orbital only the electrons leaving an orbital and occupying a new one are marked for clarity. The photo ionization would than look like

$$2s^2 2p^6 + \hbar\omega \rightarrow 2p^{-1}\epsilon l$$

and the Auger decay

$$2s^2 2p^6 + \hbar\omega \rightarrow 2s^{-1}2p^5 np^1 \rightarrow 2p^{-1}\epsilon l\,.$$

Lastly, it should be mentioned that experiments have found the decay mechanisms of excited quantum systems might differ for different system properties. It seems like energetically low excitations of a systems prefer to decay by photon rather than electron emission (i.e. Auger decay) [6]. While excitations of inner-shell electrons (usually high energies are needed for such excitations) are more often found decaying via e.g. an Auger decay. For very high excitations of heavy elements the most efficient decay process is the emission of x-ray photons. Nevertheless, there is also competition between different decay mechanisms.

Fano resonances

A quantum mechanical effect of importance for the data analysis in this thesis is the emergence of resonance peaks for certain autoionization processes. This phenomenon was theoretically described by Ugo Fano and named Fano resonance after him. It can qualitatively be described as an interference between a direct ionization channel into the continuum and an indirect channel involving an intermediate, discrete and quasibound state [7].
Fano described the effect of autoionization as a configuration interaction between two quantum states one φ belonging to a discrete energy configuration and the other to a continuum of states ψ_E [8]. He argues that a system which is excited with energies higher than the lowest ionization potential I_p cannot be treated with a perturbation theoretical approach, if two different electronic states φ and ψ_E have the same total energy and the system is allowed to decay into these. The interaction of both configuration has to be considered within the model of describing transitions from an initial state $|i\rangle$ into $|\psi_E\rangle$ or $|\varphi\rangle$.
This thought was motivated by the experimental examination of autoionization processes displaying very asymmetric peaks in their spectra. Fano was

able to find a model that could describe these asymmetric peak shapes, now often referred to as Fano resonances.
The model's fundamental idea is the interaction of the configurations described mathematically by the state Ψ_E, which is a superposition of the discrete (φ) and the continuous configuration ψ_E. He derives a formula for the transition element $\langle \Psi_E | \hat{E} | i \rangle$ to explain the transition from an initial state $|i\rangle$ into the superposed state $\langle \Psi_E |$ using a transition operator $\hat{E}$ (the exact form of $\hat{E}$ is not important for the further argumentation)

$$\langle \Psi_E | \hat{E} | i \rangle = \frac{1}{\Gamma} \langle \phi | \hat{E} | i \rangle \sin \Delta + \langle \psi_E | \hat{E} | i \rangle \cos \Delta \,. \tag{2.22}$$

With ϕ accounting for the discrete state φ superposed with an admixture of continuous states ψ_E and Δ being a factor depending on the resonance energy $E_r = \langle \varphi | \hat{H} | \varphi \rangle - \langle i | \hat{H} | i \rangle$ and the width of the resonance Γ

$$\Delta = \frac{\Gamma}{E - E_r} \,.$$

From the symmetry of the sine and cosine one can see that for energies in the vicinity of the resonance energy E_r the interference of the states described in equation (2.22) will undergo a phase transition (it will be constructive on one side of the resonance and destructive on the other).
Fano, further, introduced the ratio $\sigma(\epsilon)$ between the transition probability into the superposed state $|\langle \Psi_E | \hat{E} | i \rangle|^2$ and the transition probability into an unperturbed continuum state $|\langle \psi_E | \hat{E} | i \rangle|^2$

$$\sigma(\epsilon) = \frac{|\langle \Psi_E | \hat{E} | i \rangle|^2}{|\langle \psi_E | \hat{E} | i \rangle|^2} = \frac{(q+\epsilon)^2}{1+\epsilon^2} \,, \tag{2.23}$$

where ϵ is the reduced energy variable

$$\epsilon = \frac{E - E_r}{\frac{1}{2}\Gamma} \,,$$

and q the Fano parameter

$$q \propto \frac{|\langle \phi_E | \hat{E} | i \rangle|^2}{|\langle \psi_E | \hat{E} | i \rangle|^2} \,.$$

Equation (2.23) describes the Fano resonance peak shape. The lines produced by the formula are plotted in figure 2.3 for different parameters q. The asymmetric peak shape is apparent. One can see that for $q > 0$ the destructive interference lies to the left ($E < E_r$) of the resonance energy ($\epsilon = 0$), while the constructive interference takes place to the right ($E > E_r$) of the resonance. For $q = 0$ there is only destructive interference to be observed. And for negative Fano parameters the peak shapes will be displaying constructive interference to the left and destructive to the right of the resonance energy.

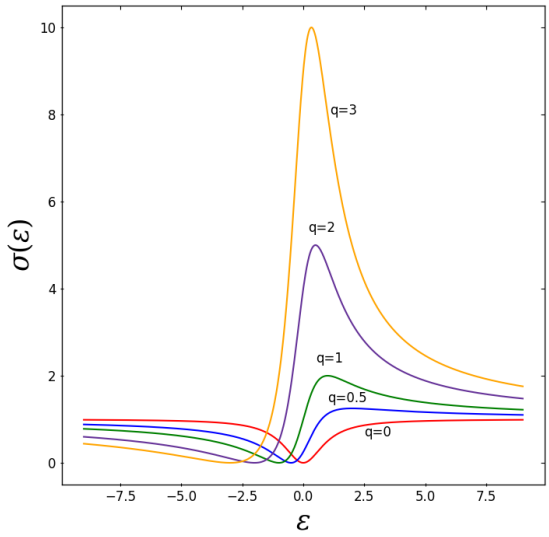

Figure 2.3: Fano resonances. The x-axis shows the reduced energy variable $\epsilon = \frac{E-E_r}{1/2\Gamma}$ depending on the exciting energy E the resonance energy E_r and the peaks width Γ. The y-axis displays the ratio $\sigma(\epsilon) = \frac{(q+\epsilon)^2}{1+\epsilon^2}$ of the Fano parameter q and the reduced energy *epsilon*. Graphs for different values of q are plotted with the respective value denoted.

Transferring Fano's theoretical approach to the example from the previous section, the neon atom, it should be expected to see such Fano resonances in an electron spectrum, when scanning the exciting-photon energy over a $2s - np$ resonance. This is due to the fact that the final states of the photoionized neon in figure 2.2a and the neon ion after the Auger decay shown in 2.2c are the same. Their emitted electron, nevertheless, will be measured

with a kinetic energy dependent ($E_{kin,photo}$) or independent ($E_{kin,Auger}$) of the incident radiation energy. Both configuration will actually be in a superposed state and interfere, creating a Fano resonance in the measured electron spectrum.

2.2 Cluster and Processes in Cluster

The sections above were dealing with electronic processes happening in single atoms or molecules and these have been studied excessively. Unfortunately, nature does very rarely provide environments with isolated atoms or molecules (especially, when one is interested in processes relevant for biological environments). In 1997, Lorentz Cederbaum proposed that more complicated interactions might take place when atoms or molecules are not isolated but rather bound together via weak forces [9]. Weak forces, here, referring to forces that are magnitudes weaker than the covalent or ionic forces that tie molecules and ions together. Such weak forces are, indeed, found often in environments of organic molecules. The most prominent example are hydrogen bonds.
Such weakly bound systems (so-called cluster) were already investigated before Cederbaum's publication. These are simply an ensemble of atoms or molecules binding together via weak forces. The number N of atoms or molecules in a cluster is usually in the order of $1 < N < 10^7$ [10]. The amount of interacting particles is less than usually referred to in solid or liquid phase matter (dense media), but, as described below, such a system will display certain interatomic/ -molecular interactions. This makes clusters a suitable laboratory candidate for examining the different properties and processes in an ensemble of particles interacting with each other in contrast to single isolated particles. Especially, clusters of rare gases are commonly used to study and understand fundamental concepts of interatomic interactions. This is, because rare gases are relatively simple atomic systems in terms of quantum mechanical calculation. Furthermore, their electronic rare gas configuration makes them easy to handle experimentally without reacting with other atoms or molecules and it is comparably easy to produce them in the laboratory [10].
Early studies have focused on ground state properties of clusters and which geometrical structures these could form. It was Cederbaum who introduced the question about excited electronic states of clusters and new decay chan-

nels opening up compared to isolated atoms or molecules. Nomenclature distinguishes between single particles as *monomers* and ensembles of particles as clusters (if the explicit size of the cluster is known and the cluster is not too big, the terms *dimer*, *trimer*, and so on are used).
Cederbaum's investigated theoretically that atoms or molecules experiencing an inner-shell excitation above the lowest ionization potential I_p but below the double ionization potential (DIP) could indeed emit a second electron, if the system was in a loosely bound state with other atoms or molecules. The argumentation is that the initially ionized monomer would not posses enough energy for ionizing another of its electrons. Though, a dimer or bigger cluster system would have a lowered DIP due to less Coulomb repulsion in the not yet ionized neighbouring particles of the cluster. This means, the excess energy after inner-shell ionizing or exciting an initial particle of the cluster, can be transferred to a neighbouring particle, which than is emitting an electron. This process is called interatomic (or intermolecular) Coulombic decay (ICD) and the emitted electron is referred to as ICD electron. The IC Decay proposed by Cederbaum is very similar to the mentioned Auger decay and sometimes called non-local Auger decay. Figure 2.4 shows a variant of the ICD, the resonant ICD (rICD).
The first to experimentally detect such a process were the groups around Marburger and Hergenhahn from Berlin and Dörner and Jahnke from Frankfurt. Both groups were able to show features corresponding to expected ICD electrons in electron spectra of neon clusters [11] and electron-ion coincidence experiments on neon dimers [12], respectively. Neon clusters are ensembles of neon atoms binding together by Van-der-Waals forces, which are based on dipole interactions between the atoms. These forces are very small (order $\approx 1\,\mathrm{meV}$) and even break up under thermal energies corresponding to room temperature. Although, this implies Van-der-Waals cluster might not play a vital role in processes of nature they, provide a great example for studying the fundamentals of ICD. Ever since then, "ICD appears everywhere" as Ouchi et al. have put it so eloquently, displaying scientist surprise about the high relevance of ICD and ICD-like processes [13]. Many publications stated that such intermolecular processes, indeed, can be seen in natural environments, like in the example of DNA repair mechanisms [14]. Moreover, new processes have been added constantly to the catalogue of interatomic or -molecular interactions [15]. In the following section two of these (the rICD and the radiative charge transfer or RCT) will be discussed in more detail.

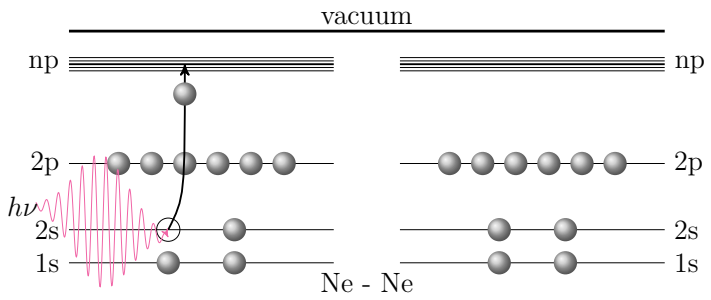

(a) Resonant excitation

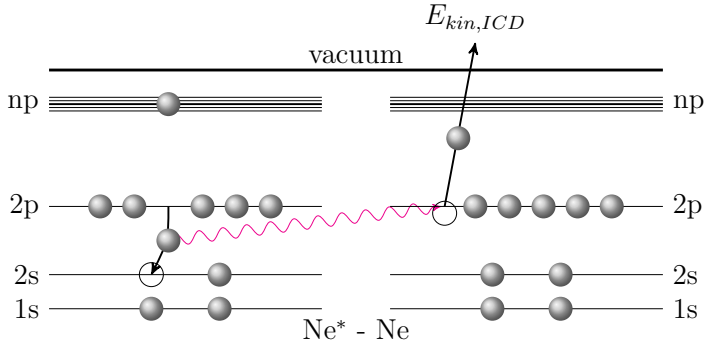

(b) ICD

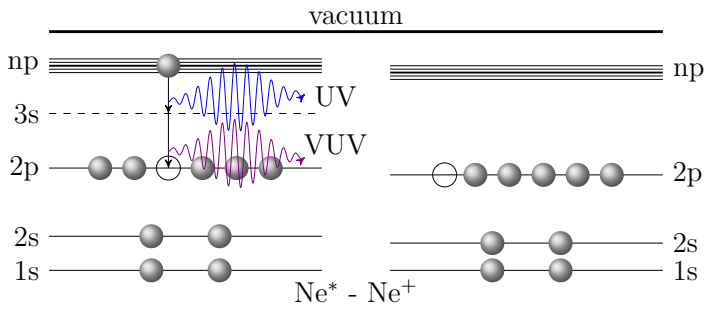

(c) Fluorescence cascade

Figure 2.4: Schematic representation of resonant ICD after excitation of a $2s$ electron in a neon clusters. The figures show two neon atoms that are bound together as a dimer. (a) shows the excitation of a $2s$ electron into a np orbital of the left neon atom. (b) shows the ICD channel, which is similar to the Auger decay shown previously, but the emitted electron is from the neighbouring neon, instead of the initially excited. An ICD electron with kinetic energy $E_{kin,ICD}$ leaves the cluster. (c) portrays the relaxation cascade of the excited electron from the np orbital over an intermediate $3s$ state into the $2p$ hole. The excess energy is released by emission of two photons (one in-between visible and UV light and one in the VUV range).

resonant ICD

In this section the resonant interatomic Coulombic decay is explained using the example of a neon dimer. The group around Barth were the first to observe this special case of ICD after a resonant excitation [16]. Figure 2.4 shows the processes following a resonant $2s-np$ excitation of one of the neons electrons. The initial excitation is analogous to the excitation explained for a single isolated neon atom (see 2.4a). Additionally to a local Auger decay the ICD channel opens up for a cluster. The initially created $2s$ hole is filled by a $2p$ electron from the same atom, as happening in the local Auger. The excess energy from this transition, though, is not passed on to the excited electron in the np state, but instead enough to ionize an electron in the $2p$ shell of a neighbouring neon atom. Figure 2.4b shows this process depicting the energy transfer by the magenta wave. With the same arguments as in the case of an Auger electron, the ICD electron's kinetic energy would not be expected to show a dependency on the exciting-photon energy $\hbar\omega$. Also, the binding energy of the electrons to their atoms in a clusters is lowered for bigger clusters and the exact cluster size is experimentally not easy to determine for bigger clusters [15], for this reason, the ICD electrons will usually create a broad feature in an electron spectrum, due to the emission from clusters of different sizes.
The interaction in-between the two neon atoms shown by the magenta wave in figure 2.4b raises some questions.Such as what exactly is the nature of this interaction? The picture painted by the theoretical description of the ICD process can be understood qualitatively considering some of the mathematical key steps. The fundamental idea is to model the interaction leading to the ICD electron emission using the same formalism as used for Auger decay. Both use Fermi's golden rule (2.14) in order to model the electron-electron interaction proportional to the square of a pertubative matrix transition element $|\hat{H}'_{ki[\sigma_1,\sigma_2]}|^2$. The index k is representing the outgoing electron wave orbital, i the initial inner valence vacancy and $\sigma_{1/2}$ the final outer valance vacancies. For the local Auger decay the orbitals associated with the indices $\sigma_{1/2}$, will be located at the same atom, while this is not the case for the ICD. Further, the antisymmetric wave function of the electron will have two contribution to

$$|\hat{H}'_{ki[\sigma_1,\sigma_2]}|^2 = |\hat{H}'_{ki\sigma_1\sigma_2} - \hat{H}'_{ki\sigma_2\sigma_1}|^2 \,. \tag{2.24}$$

These contributions are named direct term ($\hat{H}'_{ki\sigma_1\sigma_2}$) and exchange term ($\hat{H}'_{ki\sigma_2\sigma_1}$), which represent two different possibilities of the ICD process.
The direct term is interpreted as the energy transfer between two atoms as figure 2.4b shows and has been explained in the description of the figure. The mathematical description of the energy transfer in this term is described as a Coulomb interaction between the electrons of the different atoms. For this reason the term *virtual photon* is often read in literature to describe the ominous interaction.
The exchange term can be interpreted as a literal electron transfer between the atoms of a cluster. In the case of rICD in neon dimers the exchange term would correspond to a filling of the initially created $2s$ hole by a $2p$ electron from a neighbouring atom and a sequential ionization of the initially excited electron in the np state.
For deeper inside into the mathematical formalism of interatomic processes it is referred to literature [15], [17]. The exchange term describing the ICD rate (equation (2.24)) is not depicted in figure 2.4, because it can be neglected. This is due to the fact that the direct term is modelled using dipole-dipole interaction (scaling with $\propto 1/R^6$ for the distance R between the dipoles), while the exchange term depends on the overlap of the involved electrons' wave function (scaling with $\propto e^{-R}$) [15]. Thus, for mean distances between the atoms in a cluster, the direct term is dominating over the exchange term, which has been confirmed experimentally, as well [18].
Lastly, figure 2.4c shows a photon cascade with which the still excited neon dimer will decay into the energetic ground state after the ICD process. The excited electron in the np state will undergo a transition trough a $3s$ intermediate state into the $2p$ orbital, releasing two photons [19]. One of the photons will be in the range between visible and ultra violet (UV) light, while the other carries the energy of a VUV radiation (vacuum ultra violet, the range of UV light for which matter is not transparent any more).

Radiative Charge Transfer (RCT)

Yet, another interatomic process that will be of relevance for the data analysis in this thesis is the so-called **R**adiative **C**harge **T**ransfer. A rough schematic explanation of this relaxation mechanism is shown in figure 2.5. For this purpose heterogeneous neon-krypton cluster were investigated, because the RCT channel opens up already above the neon $2p$ ionization threshold I_{2p}, while in homogeneous neon clusters only after a doubly ionized atom is cre-

ated within the cluster (see figure 2.5) [20]. The figure shows a neon atom with a $2p$ electron hole loosely bound to a krypton atom. For the krypton atom only the $4p$ outer valence shell is shown here neglecting the energetic underlying fully occupied orbitals, which are not involved in the decay for clarity. The $4p$ orbital of krypton possesses a slightly lower binding energy than the $2p$ orbital of neon. Therefore, the energetic ground state of the cluster is retrieved, when a $4p$ electron is transferred from the krypton to the neon, as shown in figure 2.5. The excess energy is emitted via an UV photon and the heterogeneous dimer is left behind with a neutral neon atom and a singly positively charged krypton ion.

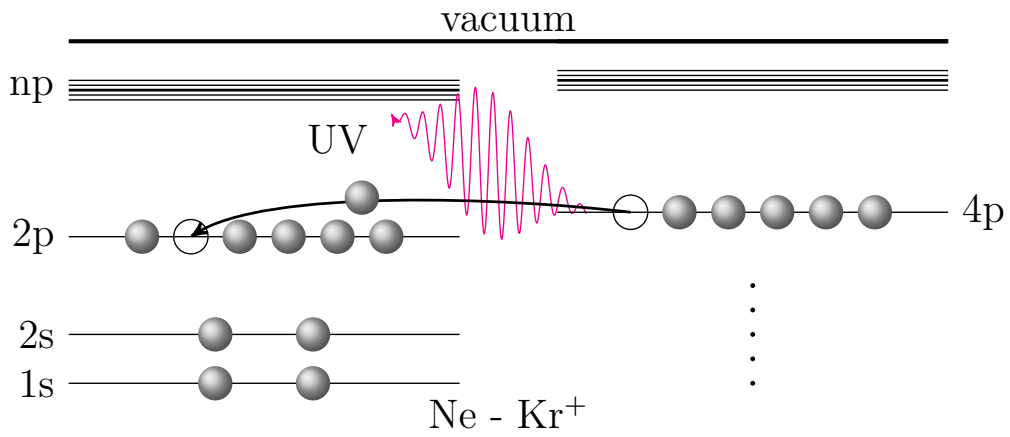

Figure 2.5: Scheme of a neon-krypton cluster undergoing charge transfer. The $2p$ electron hole in neon can for example be achieved by direct $2p$ ionization or by Auger decay. In order to restore the energetic ground state of the cluster system an electron will transfer from the $4p$ shell of krypton to the neon atom an fill up the $2s$ hole. The excess energy of this process is emitted via an UV photon for this case.

Considering the state $2p^{-1}$ of the neon atom prior to the RCT, it was already discussed that this configuration can be reached via two different pathways after excitation with photon energies in the vicinity of $E_{r,np} \approx 47\,\mathrm{eV}$. As explained using figures 2.2, the neon atom can either be directly $2p$ photoionized or a $2p$ hole can be created by Auger decay following a resonant excitation. This means, the RCT photon will come coincidently with either a photoelectron or an Auger electron displaying the respective distinct kinetic energies. This ought to be kept in mind for later argumentation.

2.3 Experiment

This section will go over the concepts needed to follow data acquisition. It will explain the fundamental concepts of fluorescence spectroscopy and coincidence experiments. Technical details about will be spared and can be more closely examined in the provided literature, since the main interest of this work lies in the data analysis rather than data acquisition.
The experiments were carried out at the beamline UE112-PGM1 of the synchrotron radiation facility *BESSY* in Berlin. In a synchrotron the phenomenon of *Bremsstrahlung* of accelerated charges is exploited in order to create highly focused light beams over a wide energy spectrum. The beamline UE112-PGM1 provides low-energy X-rays in a range of $17 - 690\,\mathrm{eV}$ and an energy resolution in the observed energy range of $\delta E < 5\,\mathrm{meV}$ [21]. The photon flux for this energy range is $> 10^{12}$ photons/s and linear and elliptical polarization is possible.
An optical assembly coupled to the synchrotron allows a selection of monochromatic light and the end-station of the beamline is not fixed, such that the monochromatic synchrotron radiation can be used by external users mounting their experimental chambers onto the last beamline valve. The focus of the optical arrangement lies roughly one meter behind this valve and there is enough space for relatively large experimental set ups.
Two of BESSY's operational modes are used in the experiments presented here. The multi bunch mode, which is the most common mode at BESSY and contains multiple electron packages in the storage ring at once creating fast consecutive photon pulses. The single bunch mode on the other hand is better suited for time-resolved measurements, since only a single electron bunch is stored at the synchrotron. This single bunch produces light pulses with a greater time interval in-between than the multi bunch mode. More information on synchrotron sources and their radiation in general can be found in numerous books such as [22] or explicitly for BESSY's beamline UE112-PGM1 in publications like [21].

The detectors used to measure photons and electrons are based on multi channel plate (MCP) stacks [23]. Electrons hitting these plates release further electrons from its surface, which will be accelerated through channels within the plates using an electric field. On their way through the plates the electron knock out process is repeated creating an electron avalanche. This avalanche can be measured as an electrical signal, which is propor-

tional to the incoming amount of electrons and thus also proportional to the initial amount of particles triggering the avalanche. The sensitivity of the multi channel plates lies in the order of single particles. For electron detection these MCPs can be used plainly. For photon detection some MCPs are covered by a window or have a coating on the upper most plate, which is designed to release electrons when excited by incoming photons of certain energy ranges [24]. For the performed measurements three different photon detectors were used. One was sensitive only in the vacuum ultra violet (VUV) range $\lambda < 130\,\mathrm{nm}$ and referred to as VUV detector. This detector has no window or coating and consists of a simple MCP stack. Its anode measuring the electrical impulse of the electron avalanche is sensitive to the position of the incoming electron cloud and uses a *wedge and stripes* arrangement [23]. The second detector spans a spectral range of $150\,\mathrm{nm} < \lambda < 600\,\mathrm{nm}$ and is here called VISUV, because of the energy sensitivity ranging from UV into the visible regime. The detector was produced by *RoentDek* and posses a position sensitive hexagonal delay line anode and a fused silica window in front of the photocathode MCP which is coated with bialkali layer in order to create a sufficient electron release in the energy range of interest. The last detector is a *RoentDek* detector, as well and will be referred to as UV detector, since it is sensitive in the energy range of UV light $115\,\mathrm{nm} < \lambda < 300\,\mathrm{nm}$. The UV detector is equipped with a hexagonal delay line cathode. The cathode is coated with caesium telluride and has a magnesium fluorid window [23].
The MCP signal is read out in reference to the bunch marker signal from BESST by data acquisition hard from RoentDek [25]. Lastly, the fundamental techniques of the used cluster production source can be followed in the literature [26]. Nonetheless, it should be noted, that the cluster source consists of cooling system for the gas phase medium and surrounding an expansion chamber from which the gas expands through a tiny nozzle (magnitude µm) into another evacuated chamber (cluster chamber). The transition of the gas from high pressure within the tubes of the source into the vacuum combined with the cooling of the source, creates a very narrow velocity distribution of the gas atoms. This means the gas atoms have very little velocity components relative to each other, or one could say, the gas cools down. The effect is the same as found in a deodorant can, which is stored at room temperature, yet, the gas that flows out of the nozzle is evidently cooled down. With sufficiently high pressure differences this type of adiabatic expansion is called super sonic expansion resulting in a highly focused and low tem-

perature beam of gas. Is the temperature low enough (below the point that the relative kinetic energy between particles is not enough to break up the bonds created by weak forces like van-der-Waals forces) clusters can form in the beam. Within the beam monomers and clusters will coexist and the mean cluster size depends on source parameters like temperature, pressure, nozzle size and shape. Besides, the axis along the center of the cluster beam provides the best environment for cluster formation. This can be expressed by the ratio η of clustered molecules to monomers found in the beam. This ratio will decrease with the distance r from the central axis.
The created cluster beam is than led through a skimmer into a second chamber, the interaction chamber. The skimmer serves the purpose to maximize the ratio η by cutting out regions of lower monomer to cluster ratio from the beam. Within the interaction chamber the cluster beam is crossed it with the synchrotron beam.
Vacuum is guaranteed using turbo molecular pumps which are installed at each chamber.

Fluorescence Spectroscopy

Fluorescence spectroscopy describes the interrogation of matter by detecting light emitted from it. This is done in fluorescence spectroscopy after an initial excitation of the examined medium. The excitation can be achieved by electron impact or photon irradiation. From the detected emission, statements about electronic configurations and transitions can be made by comparison to theoretical calculations. For this purpose it is useful (but not necessary) to detect the fluorescence emission spectrally resolved [27] [10].
The working group of professor Ehresmann has specialized on fluorescence detection of cluster processes [28]. This experimental methods has certain advantages in contrast to the charged particle detection, which is most common in research for cluster specific decay processes. The mean free path of photons travelling through matter, for example, is larger than the mean free path of charged particles (due to larger mass and the charge enhancing the probability of these particles to interact with their environment). Fluorescence detection has been used by the Ehresmann group to determine the absoluts cross sections of cluster-specific decay mechanisms [29], the photo cascade following resonant ICD in neon dimers (as shown in figure 2.4c) [19] or to collect evidence for the RCT decay channel in heterogeneous Ne-Kr clusters [20],[30], to name a few examples.

Figure 2.6 shows a scheme of the experimental set up used for the measurement. The synchrotron radiation is focused onto the cluster beam in the interaction chamber. The photon detectors are positioned around this interaction region. The two chambers containing this set up and the needed data acquisition and vacuum hard ware is built mobile for the transport to different synchrotron facilities. It is further referred to as photon induced fluorescence spectroscopy (PIFS) set up. Figure 2.6 shows how the basic concepts of the PIFS are arranged.

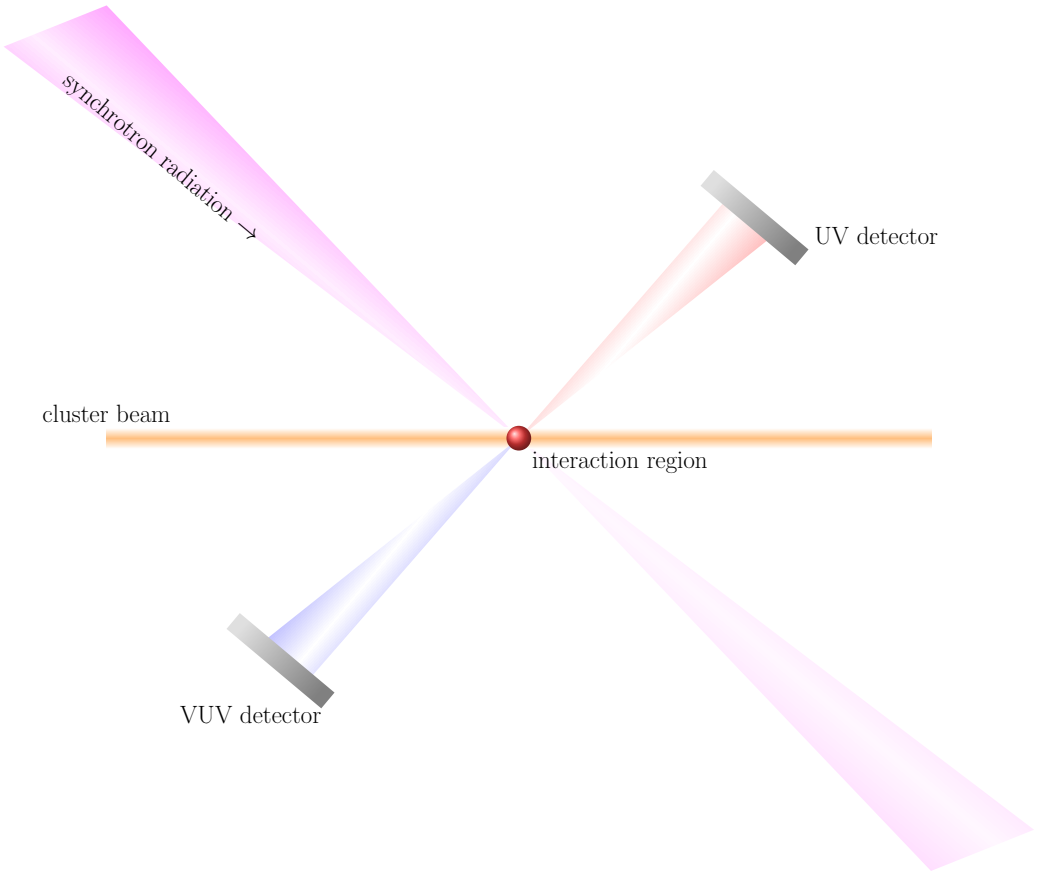

Figure 2.6: PIFS set up used for the fluorescence detection in cluster experiments. The radiation produced by the synchrotron is crossed with a cluster beam produced in a cluster source. The crossing point is noted as the interaction region. Fluorescence is emitted from this region by the excited particles in the beam and measured using the VISUV and VUV photon detectors.

The PIFS set up can also detect dispersed fluorescence emission by introducing a spectrometer with a grating before the photon detector. For the experiments presented here, the spectrally resolved detection was not utilized. The VISUV and VUV were used collecting the photon count of the respective photon energy range. Solely the integrated signal over their detector surface is examined the information on the position on the detector, as well as the angular distribution of particles from the interaction region is disregarded.

2.3.1 Coincidence Experiments

Coincidence experiments are experiments in which multiple particles produced in the same interaction are detected. There are certain advantage of such detection methods. The de-excitation pathways of excited atomic or molecular systems are usually consisting of competing processes, each producing charged particles or photons. Not rarely, the combination of created particles and their kinetic energy during a de-excitation process is specific for a certain decay channel. This is, especially, true for cluster systems. The simultaneous detection of multiple particles created in an (inter-)atomic or molecular process, therefore, provides intriguing insights in these processes and helps distinguish between different channels [31]. Coincidence experiments were mainly carried out with charged particles, since these can be guided to detectors by magnetic or electric fields. Neutral particles (i.e. photons), on the other hand, can not be guided and have to "hit the detector by chance" when they are emitted in the direction of the it. This results in smaller detection probabilities since only the events emitting photons under a small solid angle are detected. In the case of the PIFS set up used the detectors are placed roughly $d = 0.35\,\mathrm{m}$ from the interaction region and have an radius of $r_D \approx 0.02\,\mathrm{m}$, which leads to a measured solid angle $\Omega_{\mathrm{photon}} \ll 1\%$ of the total solid angle for photons [25].
A VUV and a magnetic bottle time-of-flight electron spectrometer [32] were used. The magnetic bottle consists of a coil and a permanent magnet, which are aligned around the interaction region and an MCP stack (see figure 2.7). The magnetic field created by this arrangement can be tuned to guide near to all electrons created in the interaction region onto the MCPs mounted at the end of the coil. The coil, also, provides the function of a drift tube. Electrons will arrive at different times at the MCP stack depending on their original kinetic energy. Figure 2.7 shows the set up. In comparison to the

fluorescence set up, one of the photon detectors is replaced by the electron detector. The UV detector was used for photon detection.

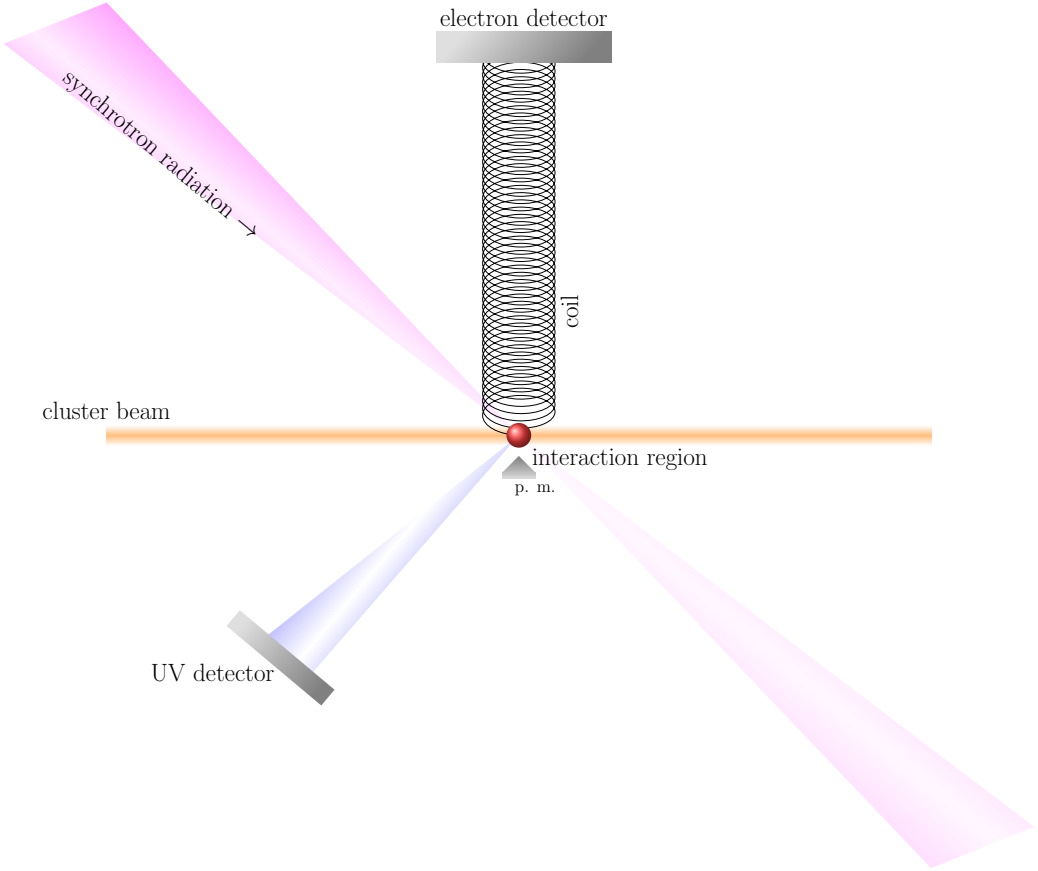

Figure 2.7: Coincidence experiment set up consisting of an electron detector and a photon detector. A cluster beam is crossed with synchrotron radiation and the electrons created in the interaction region are guided by a magnetic field (permanent magnet p.m. and coil) towards a MCP stack for electron detection, enhancing the solid angle to nearly 4π. A cmall solid angle of the produced fluorescence around the interaction region is measured in the UV range by a photon detector.

The measurement were performed at single bunch week at *BESSY II*. The bunch time intervals are $t_B \approx 800\,\text{ns}$). A bunch marker is used by the acquisition hard ware in order to correlate the detection time of the electrons with a single bunch interacting with the cluster beam. By this, the time of

flight (ToF) of the electrons could be measured, as well, as an assignment of an electron coming in coincidence with a photon could be made.
The up coming chapter will deal with the analysis of data recorded using the techniques described here.

Chapter 3

Data Analysis for RCT and rICD in NeKr Cluster

This chapter will show and explain the recorded data in more detail. For this purpose the results obtained by different experimental methods are discussed separately. The first part will deal with the experiments' outcome from a *BESSY II* beamtime, which concentrated on measuring fluorescence signals from NeKr Cluster. In this part, the raw data are shown and the argumentation for following the analysis steps are given.
In the same manner, the data recorded during coincidence experiments with NeKr cluster, also at *BESSY II*, are presented in the second section of this chapter.

3.1 RCT in NeKr Investigated Using Fluorescence Spectroscopy Data

As explained in the background chapter the data were recorded using the home-built PIFS setup. Photon intensities were observed within two different energy ranges (UV-visible and VUV). The cluster beam consisted of heterogeneous neon-krypton clusters.

3.1.1 Overview of the Recorded Fluorescence Data

Measurements were carried out varying the exciting-photon energy and detecting fluorescence emission from the neon-krypton cluster beam. The de-

tectors were position-sensitive respective to the measured photon's position on the detector surface. The photon signals were integrated over the whole detector's surface for each energy step of the scan in order to obtain the undispersed photon yield.

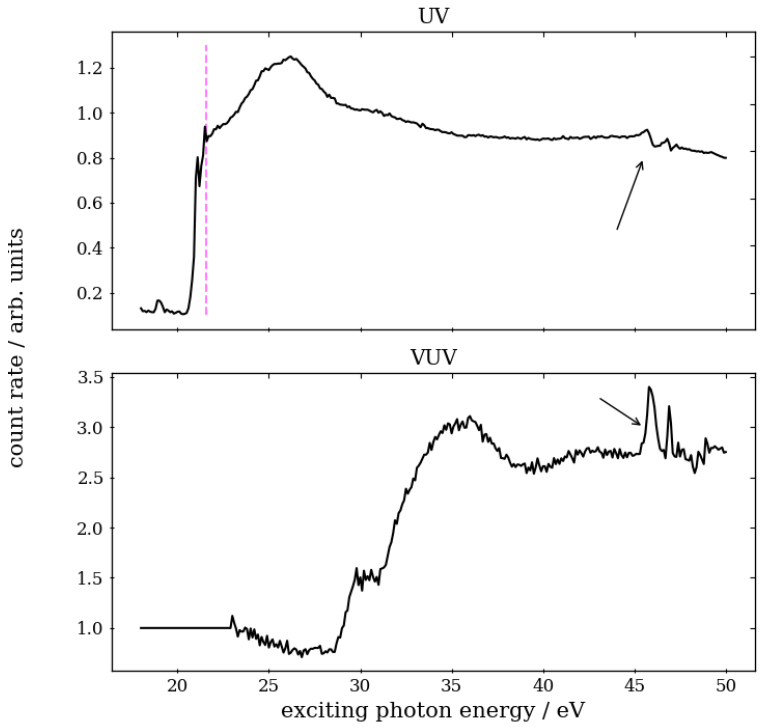

Figure 3.1: Fluorescence data recorded with two detectors. One was sensitive for UV radiation (upper panel), the other in the VUV domain (lower panel). The y axis shows the count rates of the detectors normalized using the synchrotron beam's mirror current. The x axis shows the exciting photon beam's energy, which was scanned from just under 20 eV up to around 50 eV. The VUV detector is not sensitive any more in the lower energy region of the scan. The UV detector displays the $2p$ absorption edge of neon at around 21.5 eV (magenta line). Resonant features, attributed to rICD and RCT, can be seen at the high energies (arrows).

The main interest was this integrated fluorescence intensity for the energetic

region around the resonance energy $E_r \approx 47\,\text{eV}$ corresponding to the $2s \rightarrow np$ transition as described in section 2.1. Figure 3.1 shows a scan over a greater energy range between 18 and 50 eV. The photon detector count rate is shown for the UV detector (upper panel) and the VUV detector (lower panel). Also, the mirror current, which is a reference for the synchrotron's beam intensity and, therefore, proportional to the measured fluorescence signal was detected and used to normalize the photon yield (the raw photon count and the mirror current are shown in the appendix A.1).
Features towards low exciting-photon energies in the VUV signal (lower panel) are in an energy range, where the detector was probably not sensitive for the incoming-photon energy any more. Thus, features below $\approx 25\,\text{eV}$ (see A.1) are discarded for the VUV signal displayed in figure 3.1.
The UV signal shape in figure 3.1 does posses the expected shape for the cross section of atomic neon as it was mentioned in the background chapter. The $2p$ ionization edge can be seen as it would have been expected around $I_{2p} = 21.56\,\text{eV}$ (magenta dashed line in the upper panel). This fluorescence signal is due to neon atoms in cluster and monomers coexisting in the cluster beam. These are ionized as soon as the exciting-photon energy exceeds I_{2p} and emit photons when recombining with free electrons. As expected and seen in literature ([6]) the cross section abruptly rises at the absorption edge reaching a peak quickly. For higher photon energies the cross section decreases slightly.
The features of interest for investigating cluster specific processes are located around $E_r \approx 47\,\text{eV}$, which are indicated by the arrows in figure 3.1. These peaks lie on the atomic background signal, which was just discussed. Compared to this signal the peaks are small, which fits the small condensation rate of clusters in a beam (depending on the parameters set at the cluster source, monomers often dominate the beam). Also, multiple features seem to be identifiable matching the expectation to see the transitions $2s \rightarrow np$ with $n \in [3, 4, 5, ...]$. In order to investigate the mentioned structure in the signal, the following analysis will concentrate on more detailed measurement for a smaller energy range $E \in [44.5, 48.5]\text{eV}$ explicitly around the resonance energies (see figure A.2 in the appendix for the photon yield of this measurement normalized to the respective mirror current).
The statistics for this measurement are not high enough to point out more than three peaks, nevertheless, it seems obvious that the peak shapes for the two detectors are not identical (see figure A.2 and 3.2). The VUV signal exhibits Gaussian-like symmetries of the peaks.

The UV detector signal, on the other hand, shows rather asymmetric peaks and the peaks seem shifted to lower energies compared to the VUV signal. These asymmetric peaks will be discussed in more detail in the next section.

3.1.2 Fitting of the Resonance Features

The section about Fano resonances in the background chapter (3.1.2) gives an insight about theoretical description of certain types of asymmetric features in electron spectra. These features appear due to an interference between the outgoing electron wave function of two different processes resulting in one and the same final energy state of the system. The quantum systems described in the presented example are neon-krypton clusters, the same as is observed here experimentally. The interfering processes mentioned are, firstly, the direct photoionization of a neon atom in a heterogeneous Ne-Kr cluster resulting in a photoelectron and a UV photon, which is emitted by the consecutive RCT. And, secondly, the resonant excitation of a Ne $2s$ electron into a np shell, which is followed by an Auger decay emitting an Auger electron and, again, the RCT emitting an UV photon. Both processes end up in the same final state $Ne + Kr^+$ and both processes emit an UV photon and an electron. The electron is, in the first case, described by a continuous distribution of eigenstates (depending on the exciting-photon energy), while in the latter process only discrete eigenstates are possible resulting in defined electron energies independent of the exciting-photon energy.
The argumentation for the presented data is as follows. The interference, described by Fano's formula for electrons, is quantum mechanically entangled to the consecutively emitted photons of the two processes. Which means, the UV fluorescence spectrum should contain peak shapes resembling Fano resonances, as well, whereas, the VUV detector should not show any asymmetric peak shapes, because only the photons that are emitted by the photon cascade following rICD (compare 2.4) should be found in the energy region covered by the VUV detector.
The data represented in A.2, indeed, show characteristics that would match the argumentation above.

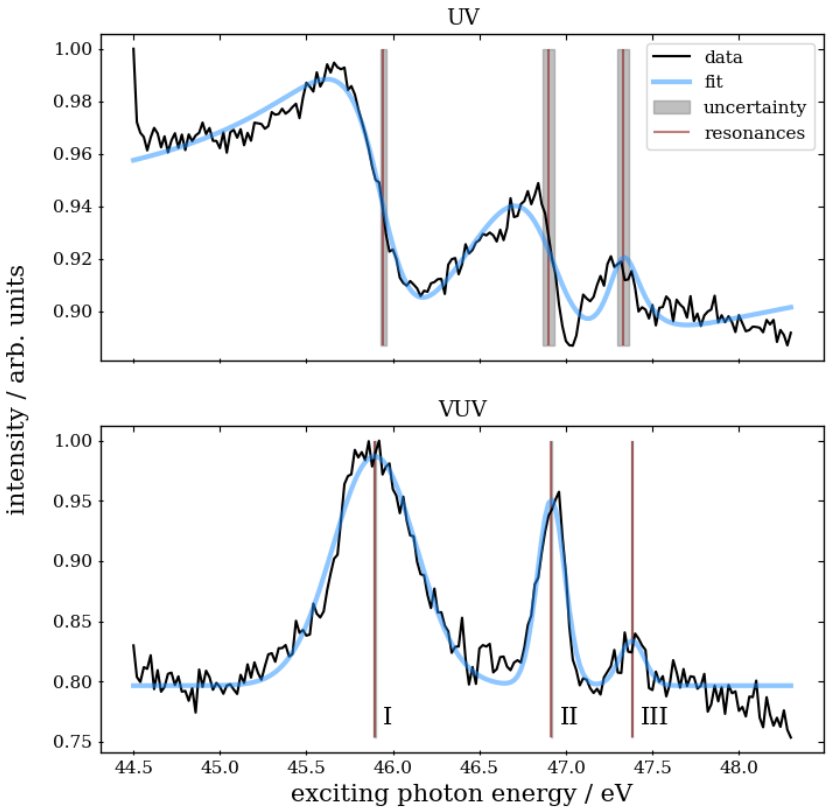

Figure 3.2: Multifit of a series of Gaussian curves to the VUV data (lower panel) and multifit of a series of Fano resonances to the UV data (upper panel). The position of the resonance determined by the respective fits are shown as vertical lines in the graph.

In order to improve the evidence for this, the VUV and UV data are fitted with appropriate functions and the position of the resonance peaks are determined from the fit parameters. A sum of Gaussian curves $g_i(\hbar\nu)$

$$G(\hbar\nu) = g_1(\hbar\nu) + g_2(\hbar\nu) + g_3(\hbar\nu) + c \tag{3.1}$$

is used to model the VUV signal. Each Gaussian is of the form

$$g_i(\hbar\nu) = a_i e^{-\frac{(\hbar\nu - E_{r,i})^2}{2\sigma_i}} \tag{3.2}$$

and corresponds to a peak at resonance energy $E_{r,i}$ in the data. The UV signal can be fitted with Fano's formula for the resonance asymmetric features (equation (2.23)). This is done similarly by a superposition of three Fano curves

$$F(\hbar\nu) = f_1(\hbar\nu) + f_2(\hbar\nu) + f_3(\hbar\nu) + c\,, \tag{3.3}$$

where the mathematical description of Fano's curves from equation (2.23) is re-written slightly with the definition of the reduced energy variable ϵ and an additional fitting parameter σ accounting for the amplitude

$$f_i(\hbar\nu) = \sigma_i \frac{\left(q_i + \frac{\hbar\nu - E_{r,i}}{\Gamma_i/2}\right)^2}{1 + \left(\frac{\hbar\nu - E_{r,i}}{\Gamma_i/2}\right)^2}\,, \tag{3.4}$$

with $i \in [1, 2, 3]$. Further, the data points are normalized to posses a maximum value of one in order to reduce the amount of fitting parameters needed. It is expected to find the resonances for both signals at the exact same energetic location, since both (Fano's description of the interference and the rICD) depend on the location of the resonance energies E_r for transitions $2s \rightarrow np$. Figure 3.2 shows the data with corresponding fits.
The figure displays the measured data (black) and the fitted curves (blue), as well as the position of each resonance peak (labelled with I, II and III). The gray area around the resonance position in the UV signal (upper panel) represent uncertainties of the fit parameter $E_{r,i}$. These are also plotted in the lower panel for the VUV signal, though, the uncertainties are comparably small here and difficult to see.
The resonances of both fits match relatively well, especially considering the uncertainty of the Fano's fit. The exact fit parameter obtained are shown in table 3.1

Table 3.1: Fitting parameters obtained from the optimized curves shown in figure 3.2. The abbreviation *a.u.* standing for arbitrary units, which is used, if the value was not quantitatively relevant for the further analysis.

fit parameter Fano	Peak I	Peak II	Peak III
E_r / eV	45.945(19)	46.90(18)	47.33(19)
Γ / eV	0.62347(19)	0.70(11)	0.268(5)
q / a. u.	1.160 (10)	0.74(4)	-0.05(4)
σ / a.u.	-0.04124(17)	-0.0477(7)	-0.0391(5)
c / a.u.		1.0562(5)	
fit parameter Gauss			
a / a.u.	0.115(4)	0.0304(15)	0.0068(15)
E_r / eV	45.894(6)	46.9143(4)	47.381(16)
σ / a.u.	0.2417(7)	0.079(5)	0.073(17)
c / a.u.		0.7965(16)	

Looking at the fit parameters the resonance positions in both signals for the second (II) and third resonance (III) do not differ significantly. The resonances for the first peak display a small difference between VUV and UV signal, which is not covered by the uncertainties. This might be due to the fact that only statistical uncertainties of the fitting are considered here, while systematic uncertainties (e.g. inaccuracies during measurement) are not included.
From the *NIST* database [33] one can find the atomic resonance position and compare the experimental energy calibration to these values using the slit current. This, indeed, shows that the atomic resonances for neon lie where literature suggests and is shown in the appendix (A.3).
Also, neon $2s$ excitations of cluster have already been investigated before using electron spectroscopy ([34]). Compared to atomic signals, the cluster resonances are energetically shifted and it is stated that the $2s \rightarrow 3p$ transition is not observable. One can compare the values $E_{r,n,clust}$ from Flesch et. al. ([34]) to the values obtained by fitting in order to assign the resonant features. Here, n denotes the resonant transition into the np state

$$
\begin{aligned}
E_{r,3,clust} &= 46.27\,\mathrm{eV} \\
E_{r,4,clust} &= 47.08\,\mathrm{eV} \\
E_{r,5,clust} &= 47.54\,\mathrm{eV} \\
E_{r,6,clust} &= 47.79\,\mathrm{eV}\,.
\end{aligned} \tag{3.5}
$$

Looking at the resonance energies $E_{r,i}$ determined by fitting (3.1) and the literature values for atoms (A.1) and for clusters (3.5), it is difficult to assign the measured peaks accurately. It is known that the resonance energy shift towards lower energies for increasing cluster size and including the previous observation of the $2s \rightarrow 3p$ transition missing in cluster, the peaks can be assigned as follows

$$E_{r,1} = (45.945 \pm 0.019)\,\mathrm{eV}: \quad 2s \rightarrow 4p \tag{3.6}$$

$$E_{r,2} = (46.90 \pm 0.18)\,\mathrm{eV}: \quad 2s \rightarrow 5p \tag{3.7}$$

$$E_{r,3} = (47.33 \pm 0.19)\,\mathrm{eV}: \quad 2s \rightarrow 6p\,. \tag{3.8}$$

As can be seen, the assignment is not corresponding well to the values by Flesch et al. While $E_{r,2}$ and $E_{r,3}$ could, as well, be assigned to the transitions $2s \rightarrow 4p$ and $2s \rightarrow 5p$, respectively, the measured peak $E_{r,3,atom} < E_{r,1} < E_{r,3,clusters}$ lies between the literature value of atoms and clusters. Within their confidence interval $E_{r,2}$ and $E_{r,3}$ are, actually, identical with $E_{r,4,clust}$ and $E_{r,5,clust}$. Nevertheless, the fit parameter for the resonance energy $E_{r,1}$ is significantly different from both $E_{r,3,atoms}$ and $E_{r,3,clust}$. Taking this into account, the assignment (3.8) seems most plausible. Additionally, the energetic shift of the resonances within a cluster depends on the cluster size, therefore slight differences in the absolute quantity of the resonances between this work and literature (like [34]) could be explained by examination of differently sized clusters. The qualitative behaviour of the energy shifts remains the same. Flesch and colleagues described a blue shift of the lowest $2s$ excitation ($2s \rightarrow 3p$) and a red shift for all higher excitations, when comparing atomic and cluster signals. This can be seen here, as well.

3.2 rICD Signal in NeKr Cluster Coincidence Data

This chapter will present the data recorded at a *BESSY II* beamtime in February 2018. The PIFS setup in combination with a magnetic bottle (shown schematically in figure 2.7) was used to measure photons and electrons in coincidence.

3.2.1 Overview of Recorded Coincidence Data

As mentioned in the experimental setup section, the incoming particles on the detectors are correlated by analysis software in order to assign them to a certain synchrotron bunch. This is achieved by a detection of the arrival time of the particles at the detector after a synchrotron bunch hit the interaction region. By doing so photons and electrons that came within a certain time interval after a synchrotron bunch are saved as coincident signals. The measured time of flight (ToF) of the electrons presents information about their kinetic energy.
The analysis software distinguishes between single detected particles (electrons E or photons P) and combinations of up to four particles in coincidence within the same synchrotron bunch (electron-electron EE, electron-photon EP, photon-photon PP, electron-electron-electron EEE, electron-electron-photon EEP, and so on). The order of detection doesn't play a role, since photons will be detected more or less instantaneously after their creation in the interaction region, while the electrons' ToF will depend on their kinetic energy E_{kin} inherited from their process of origin.
The coincidence map showing the time of flight of electrons and the photon signal for EP coincidences measured with homogeneous neon clusters and exciting synchrotron energy $\hbar\nu_{\text{off}} = 46.8\,\text{eV}$ is shown in figure 3.3.
The figure consists of three graphs. The central quadratic area is the coincidence map. This map displays dots at certain positions corresponding to a coincident electron-photon pair. The coordinates on the map show the electron's ToF and the photons detection time. The map shows a certain symmetry. This is because the map was created using two consecutive synchrotron bunch excitations. This means after one bunch length $t_b \approx 800\,\text{ns}$ the signal in the map corresponds to the following bunch and always two consecutive bunches are stored in the same dataset array. The data points

in the map are binned accumulating the data within a bin of $w_{bin} = 1\,\mathrm{ns}$. The upper and right panel of figure 3.3 illustrate the integrated electron spectrum and photon signal along the respective axis. The color bar in the upper right corner shows the intensity of the bins in the coincidence map.
The exciting-photon energy $\hbar\nu_{\mathrm{off}} = 46.8\,\mathrm{eV}$ lies below the resonances regarding the $2s \rightarrow np$ transitions (see literature and fitted values in section 3.1.2, equations (3.5) and (3.8)). This means, the most prominent feature expected should be the $2p$ photo electron peak in the electron spectrum with a kinetic energy of $I_{2p} - \hbar\nu_{\mathrm{off}} \approx 25\,\mathrm{eV}$. This feature can be seen in the time of flight map (3.3) as weak vertical lines at around 200-300 ns and 1000-1100 ns electron ToF. These lines are seen in the electron's integrated spectrum (upper panel) as strong peaks on the logarithmic scale.

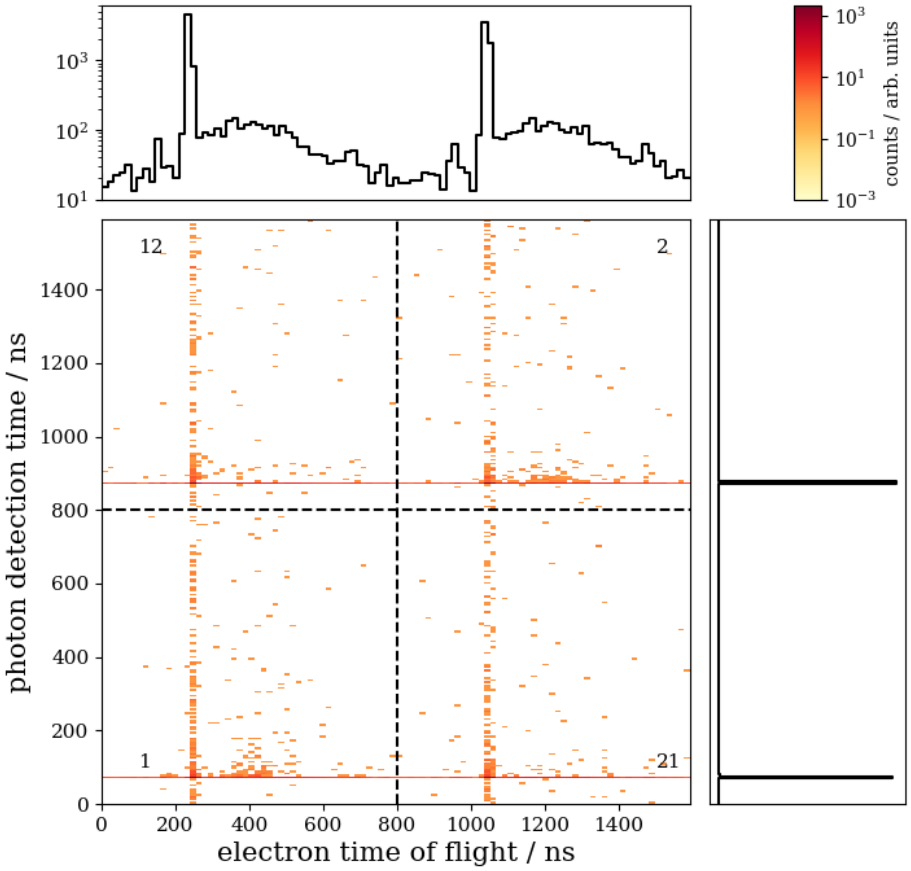

Figure 3.3: Coincidence map for electron-photon detection after off-resonant excitation of neon clusters ($\hbar\nu_{\text{off}} = 46.8\,\text{eV}$). Upper panel: integrated electron time of flight spectrum. Right panel: integrated photon detection signal.

The broad feature that appears next to the photo electron peak to longer electron ToF, consists of slower electrons with a wider distribution of kinetic energy. Such a signal is expected from theory and previous experiments ([16] ,[15]) to be created by ICD electrons (or more precisely in this case rICD electrons). These features should become more prominent in comparison to the photo electron peak for resonant exciting photon energies $\hbar\nu_{\text{resonant}} \approx$

47.05 eV. Figure 3.4 shows the coincidence map in the resonant excitation regime.
It can be seen that the broad feature next to the photoelectron peak is enhanced in the resonant excitation case (figure 3.4) when comparing it to the off-resonant map in figure 3.3. To explicitly find the energy of the electrons contained in this feature it is needed to calculate the kinetic energy from the ToF of electrons. This and further analysis of the data will be done in the following section.
The four areas separated by dashed lines in figure 3.4 are used for further analysis. It should be noted that the quadrants 12 and 21 cannot display any *true* coincidences stemming from the same synchrotron excitation bunch. This is due to the fact that data points in these quadrants correspond to particles being emitted from two different excitation processes. Thus, these coincidences do not tell anything about the processes of interest and are termed *random* coincidences. These random coincidences contribute to the statistical background signal (e.g slow electron from previous bunch measured in coincidence with a photon from the next bunch). The other two regions, 1 and 2, show the same signal, but include the true coincidences of two particles created within the same bunch. This will be used in further data processing steps.

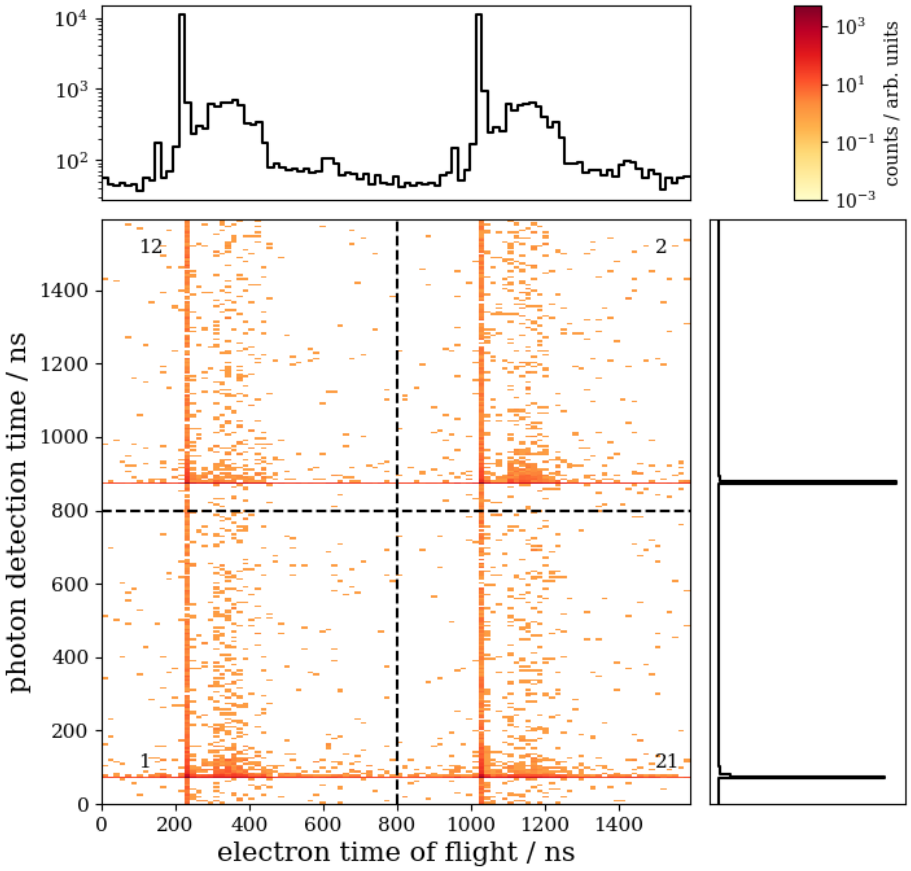

Figure 3.4: Coincidence map for electron-photon detection after resonant excitation of neon clusters ($\hbar\nu_{\text{resonant}} = 47.05\,\text{eV}$). The dashed lines marking four distinct regions. Region 1 and 2 represent the areas of the map in which real coincidences from the first and second bunch are present. Regions 12 and 21 display either random coincidences between particles from created by different bunches or statistical background, but no true coincidences from a single event of origin.

3.2.2 Analysis of rICD in NeKr Clusters using Coincidence Maps

The data presented in the previous section can be calibrated using a set of calibration measurements. The magnetic bottle uses guiding magnetic fields for the electrons. These are controlled by applied voltages to the magnetic bottle coil and its field influences the detected time of flight by accelerating and retarding the electrons. Therefore, it is necessary to do calibration measurements for each set of magnetic bottle parameters used for the actual measurements. Each measurement consists of a scan over various exciting energies. Single electron spectra are recorded, which will display a photoelectron peak from $2p$ ionized neon. The peak's position moves along the ToF-axis in dependency of the exciting-photon energy (see chapter 2.1). This dependency between exciting-photon energy and ToF of the photo electron peak is used to find a calibration function in order to calibrate the recorded ToF data to the corresponding kinetic energy of the electrons. The calibration measurements and fit of the calibration function are shown in the appendix A.0.3.
The coincidence maps calibrated for kinetic energy of the electrons can be seen in the appendix, as well, in figure A.5 in the case of resonant and off-resonant excitation. The figures show only the quadrant 1, since the calibration is done separately for the different quadrants of the ToF maps.
The figure 3.5 shows only the electron spectra (upper panel) from the calibrated maps (see appendix figure A.5) in the resonant (solid green line) and off-resonant (dashed red line) case. This allows an estimation of the previously mentioned features from the ToF maps. The most prominent peak in the electron's kinetic energy spectrum would be expected to be the $2p$ photoelectron signal. This agrees very well with the prediction for its kinetic energy $E_{\mathrm{kin,photo}} \approx 25\,\mathrm{eV}$, as can be seen in the figure 3.5. The broader feature to lower energies corresponds to the feature discussed for the ToF map. The energies of rICD electrons for neon cluster systems are already studied [16] and are believed to be in the energy range of roughly $E_{\mathrm{rICD}} \approx 1\,\mathrm{eV} - 4\,\mathrm{eV}$. Although, the resolution is not high, the feature in the integrated electron spectra of figure 3.5 next to the photo electron peak towards low energies seems to inhibit a peak around the expected E_{rICD} region (region 'I' between dashed black lines). The second region ('II') marked in the figure can most likely be attributed to scattered photoelectrons and will be discussed in the appendix. The spectra are normalized to the area beneath the curves.

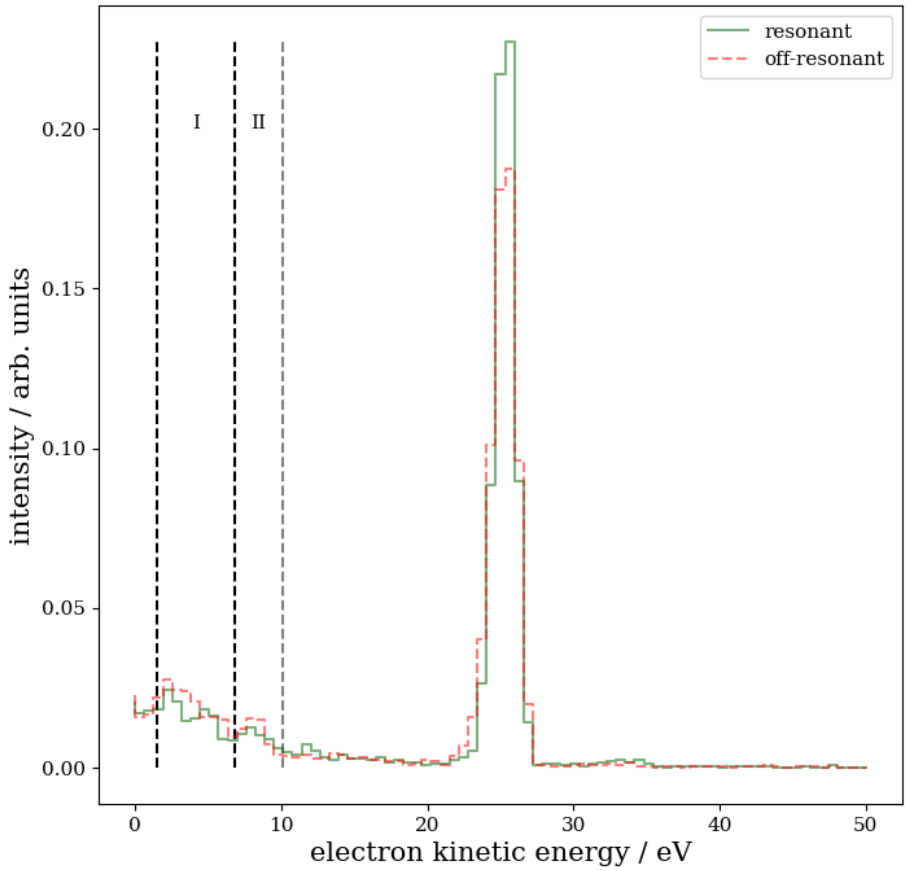

Figure 3.5: Electron spectra of electrons measured in coincidence with a photon after resonant (green solid line) and off-resonant (dashed red line) photoexcitation of NeKr clusters. The x axis shows the kinetic energy of the measured electrons and the y axis shows the normalized count rate. In the energy region denoted with 'I' rICD electrons are expected. The feature in region 'II' is believed to be due to scattered photoelectrons.

For further analysis two steps are implemented in order to enhance the rICD signal compared to statistical background. Firstly, the data are filtered for a minimum photon detection time in order to cut out the strong feature seen in the photon spectra in the right panels. This feature might be due to random coincidence events between the synchrotron beam reflected within the interaction chamber and free electrons. The filtering is done by excluding all coincidence events having shorter photon detection times than the peak in the integrated photon detection time spectrum. The value for the first bunch cut-off $c_{\text{off},1} = 74.4\,\text{ns}$ is determined by a zoom into the region of the map (figure A.7). The cut-off value for the second bunch can be calculated from the bunch length $c_{\text{off},2} = c_{\text{off},1} + t_B$.
The following figure 3.6 shows the same electron spectrum after the filter for photon detection times is applied. Comparing this figure to the previous, unfiltered spectra (see 3.5, the feature in regions 'I' and 'II' are more prominent compared to the photoelectron peak.

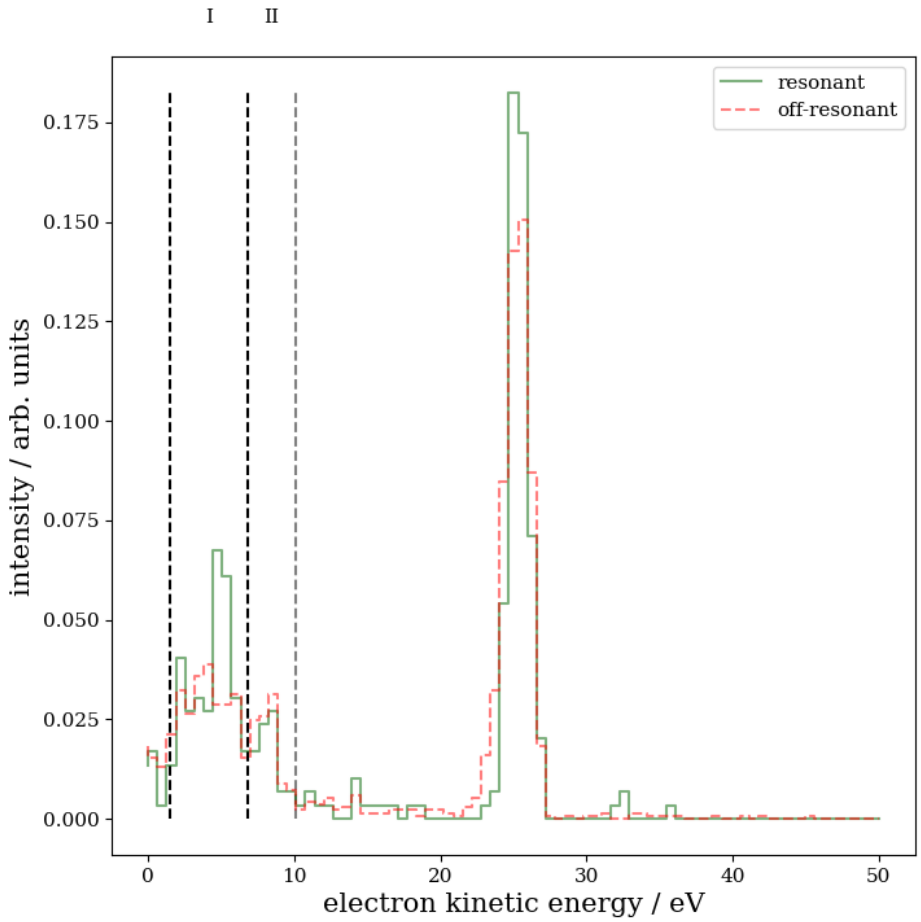

Figure 3.6: Electron spectra of electrons measured in coincidence with a photon after resonant (green solid line) and off-resonant (dashed red line) photoexcitation of NeKr clusters. Only data points with photon detection times of 74.4 ns (first bunch) and 874.4 ns (second bunch) were considered.

The second method to enhance the signal of rICD, is to sum up the separately calibrated bunches 1 and 2 of the original ToF map and subtract the bunches 12 and 21

$$M = b_1 + b_2 - (b_{12} + b_{21}) \ , \tag{3.9}$$

where M is the resulting coincidence map, which was statistically cleansed of false coincidences by summing up the data of the quadrants b_i.
This method uses the argumentation that the mentioned background signal caused by random coincidences is of statistical nature and can be found in each quadrant of the coincidence map with same probability, but the true coincidence events are only found in the quadrants 1 and 2. Therefore, by performing the calculation presented in (3.9), it is possible to improve the ratio of true to random coincidences. This, again, helps enhance the signal of a coincidence event of interest compared to more prominent processes that do not produce coincident particles.

Following the data processing steps described above, figure 3.7 is created. The photoelectron peak should be removed, because its signal would be expected to be of same intensity in each bunch b_i equalling out for the sum M. It can be seen that this is in principle the case, but the low statistics of the experiment create some leftover signal where the photoelectron peak was.
In contrast, the features attributed to coincident events (i.e. the suspected rICD peak) should be enhanced by calculating the sum M. This is due to the fact that the peak should not explicitly show in the off-diagonal bunches b_{12} and b_{21}. This result of the analysis procedure is evident in figure 3.7. Between the off-resonant and resonant excitation map there is, now, a marginal difference observable in the low kinetic energy regime of the electron spectra. The electro spectrum after resonant excitation (green solid line) displays two features in the low kinetic energy regime. The first is seen at roughly $E_{kin} \approx 2 - 5\,\mathrm{eV}$ matching the prediction of rICD electrons. The second prominent feature can be seen at just below 10 eV and is slightly vaguer than the suspected rICD signal. This peak could be identified as a feature discussed in the same earlier experiments [16]. Barth et al. explained these electrons as $2p$ photo electrons scattered within the cluster which thereby are shifted to lower kinetic energies. In addition, this claim is supported by the exciting photo energy dependency of this peak, which is expected for emitted electrons produced directly by interaction with the incoming radiation. This dependency can be observed in figure A.6 in the appendix.

It should be noted that the photo electron peak is evidently weaker than before the analysis step, even weaker than the rICD signal.

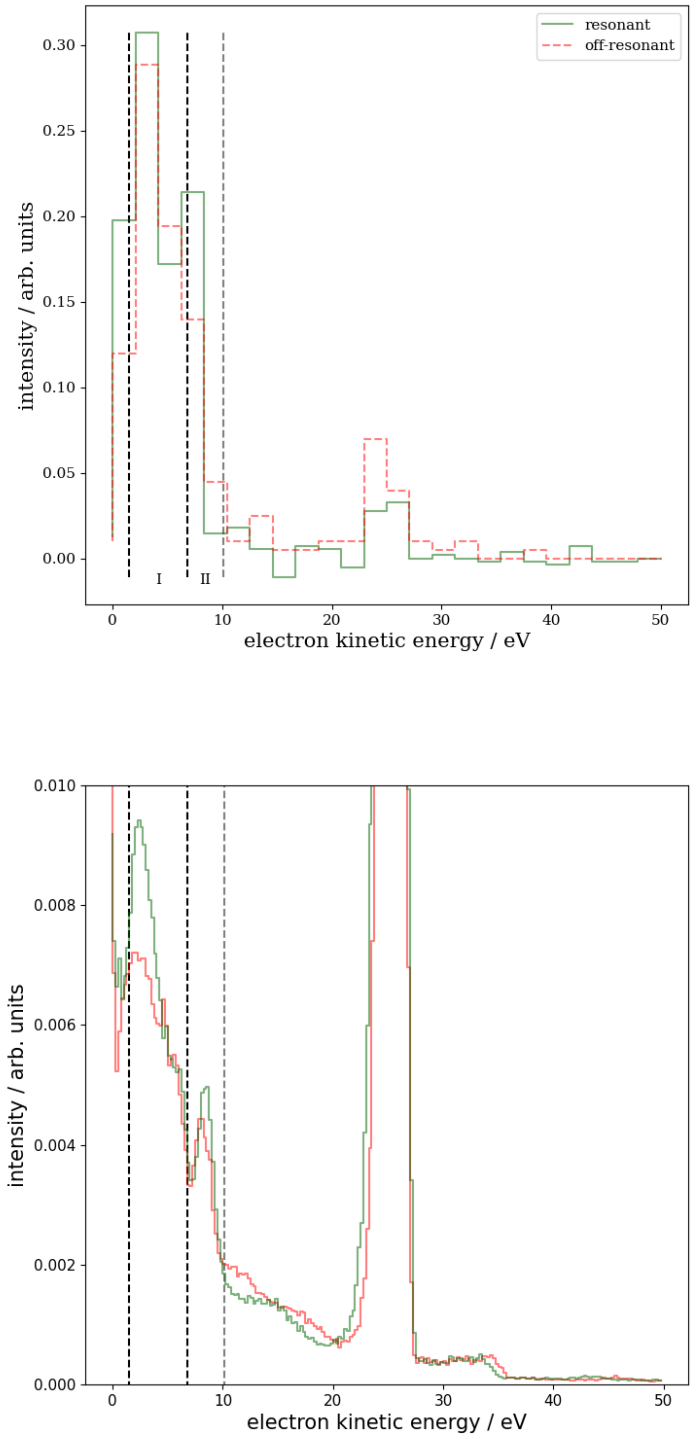

Figure 3.7: Comparison between electron spectra from singly detected electrons (lower panel) and electrons measured in coincidence with a photon (upper panel). Both panels show a spectrum for an initial resonant (green) and off-resonant (red) excitation.

In order to compare the resonant and off-resonant measurements and the coincidence data with single particle detection figure 3.7 summarizes these. The panel titled 'single electron detection' shows the electron spectra recorded for single particle detection after resonant and off-resonant excitation. The upper panel of figure 3.7 displays the electron spectra of electrons measured coincidently with photons. Both spectra are evaluated following the steps described above. All spectra were normalized in respect to their covered area being $A \stackrel{!}{=} 1$.

The single electron spectra (lower panel) show the same behaviour as was stated by Barth et al., who measured the single electron spectra, as well. The rICD electron peak (marked with 'I') is clearly becoming more prominent in the resonant excitation regime, while the second peak associated with the scattered $2p$ photo electrons (marked with 'II') is increasing only very slightly.

The upper panel shows the exact same marked regions to guide the eye. The photo electron peak ($E_{kin,2p} \approx 25\,\mathrm{eV}$) that is the dominating feature in the lower panel, is in the same order of magnitude as the rICD feature for the coincident electron spectra.

The two features in the low kinetic energy range are hard to distinguish in the coincident electron spectrum. Only with prejudice an enhancement of the rICD feature is observable. Further, the peak attributed to scattered photoelectrons (II) seems slightly stronger in the resonant case. Maybe this is an artefact of the coincidence measurements and the mentioned synchrotron reflection line in the coincidence maps. However, the statistics of the measurement is too weak in order to make any substantial quantitative claims from the presented data.

Chapter 4

Conclusion and Outlook

The data presented and fitted in 3.2 is of high interest. Although, the statistics of the experiment were not very high, it displays evidence for a correlation between emitted photons and electrons of atomic processes that has not been investigated before. Namely, the Fano-like shape of resonance peaks, that are associated with a quantum mechanical interference of different emitted electrons. It would be very intriguing to further identify, if these interferences really manifest themselves in the photon signal, too, as it is interpreted in this work.
This effect is very interesting for developing a better understanding and intuition concerning fundamental quantum mechanical processes, but also might serve as a tool that can be exploited in order to investigate different phenomena. For example, it might be possible to use this kind of interference of emitted photons on a background signal in order to determine cross sections for the underlying mechanisms. For such a procedure one first would need to identify and quantify competing process (like rICD in this case) and other parameters like condensation rates of the particles within the cluster. Further investigations using techniques described in previous analysis of fluorescence data (i.e. in [29]) might identify cross sections of radiative interatomic processes like the RCT in neon-krypton clusters.
Another possibility are dispersed photon measurements in order to have more detailed wavelength resolution. This would allow for filtering photons of specific wavelengths and eventually enhance the signal which is searched for (similarly to filtering methods presented in the chapter regarding coincidence measurements). However, technical difficulties lower the efficiency of measuring fluorescence signals compared to charged particles. These can be guided

towards the detector using setups like the magnetic bottle. But for now the statistics are too low making dispersed detection for some of these processes impractical due to way too long measurement times.
Furthermore, a theoretical modelling for the entanglement of the emitted electron's and photon's wave function would be of great use in order to validate the claim that Fano's interference mechanism manifest themselves in the RCT photon emission of neon-krypton cluster.

Even though, the coincidence data analysis demonstrated on the previous pages does not show precise evidence for interatomic processes, it is still inevitable to agree that the combination of charged particle and fluorescence detection is a strong experimental tool. The measurement of multiple bunches and the processing of these to eliminate random or false coincidences, as shown in figure 3.7, is suited to find relatively weak signals compared to the background. This can be seen by the increased signal strength of the low kinetic electrons associated with rICD compared to the photo electron peak (upper panel figure 3.7).
The evaluated experiment, however, demonstrates a weakness of coincidence experiments involving fluorescence spectroscopy, the low statistical resolution. Coincidence events underlie the mechanisms of stochastic. The detectors do not posses a perfect detection efficiency. And most of all, unlike charged particles, photons are hard to guide generally resulting in a lower solid detection angle for photons. These aspects, among others, could have been improved for the performed experiments. An immediate improvement could be a longer measuring time for collecting more events and thereby increase the signal strength of true coincidence events compared to statistical background.
A more complicated approach is to improve the solid angle of photon detection and, therefore, the probability to detect true coincidence events. This can be realized by designing some mirror setup which helps guiding the photons towards the detector. The challenge for such a construction lies not only within the needed precision during production, but also in the design of a geometry that does not interfere with the magnetic bottle. Such a setup was constructed and tested in the AGE [25]. Future improvements for coincidence data acquisition (as presented in this work) could be achieved by including this mirror.
As a last attempt to justify the ambiguity of the electron spectrum achieved from coincident electron-photon events (figure 3.7) might mention the rather

large variance for the position of resonance energies in clusters. The energy landscapes of particles bound to cluster are shifted depending on the cluster size. As seen in figure A.6, the resonance energy of the $2s \rightarrow 4p$ transition in the cluster systems seem to be just below 47.1 eV which is very close to the literature value (3.5). The size of the cluster in the experiment can vary depending on the cluster source parameters. Between the measurements shown in this work the cluster source parameters have been altered and a more precise knowledge of the these would be required to find the exact resonance energies and compare different excitation energy regimes.

Fluorescence measurements and the analysis of data recorded with such were at the heart of this thesis. The weakness due to its lower resolution compared to charged particle spectroscopy was demonstrated.
Fluorescence spectroscopy, however, brings great advantages for studying interatomic processes. The search for Fano resonances in the fluorescence signal of neon-krypton clusters demonstrated how photon signals can be used to discriminate different interatomic processes or even discover mechanism for which other methods would be blind. Here RCT could be seen in the fluorescence signal, while the emitted electrons from the previous ionization of the cluster system would be identical to atomic signals. Moreover, RCT and rICD signals were separated by choosing two detectors sensitive for different photon energies regarding the theoretical expected wavelengths of respective emitted photon. This can further be improved by introducing dispersed photon measurements.
The most intriguing outcome from this part of the analysis is the manifestation of the Fano resonances in the fluorescence spectrum. The Fano interference is thought to be an effect caused by interfering electron waves, but can apparently also be observed in other particles, in this case photons, emitted in the same process. This lead might be interesting to follow in order to gain more understanding of quantum mechanical systems and the entanglement of its constituent particles.
Further, the coincidence experiments give an insight how effective filtering for multiple particles that are supposed to be emitted by the same process can be in order to enhance a signal compared to other more prominent features. This is, explicitly, for rICD feature shown in **??**, which is the most prominent peak after the analysis steps. This means that although the experiment couldn't demonstrate an advantage in unambiguously identify the

feature when compared to the single electron spectra (figure 3.7) the methods proved themselves principally working.
The overarching goal of this thesis was the exemplary presentation of fluorescence data in general and its combination with other techniques in coincidence experiments. It was focused on the data analysis of such recorded data and successfully demonstrated which obstacles one faces. What is more, is the authors hope that also the advantages of fluorescence spectroscopy, its versatile nature and the possibility to combine it with different measurement techniques was carved out. And most importantly, that this thesis might serve as a first contact for anyone new to this topic in the AG Ehresmann.

Appendix A

Appendix

A.0.1 Mirror Current

The raw photon count of both used detectors and the mirror current recorded at the beamline are shown in figure A.1. The mirror current was used to normalize the photon count.

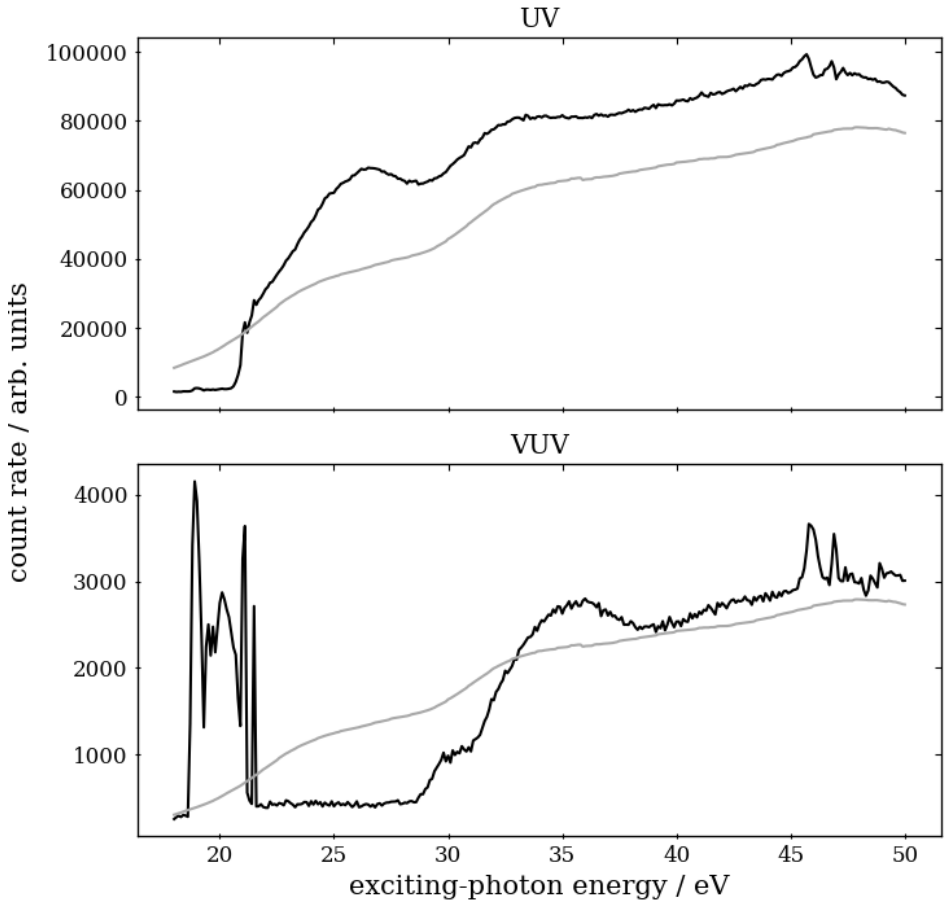

Figure A.1: Count rate of the photon detector (black lines) and mirror current (gray lines) in dependency of the exciting-photon energy. The upper panel shows the detected signal for an energy range in the UV energy range, while the lower panel shows a signal in the VUV domain.

The following figure A.2 shows a second measurement concentrating on the exciting-photon energy region around Neon's $2s \rightarrow np$ resonances.

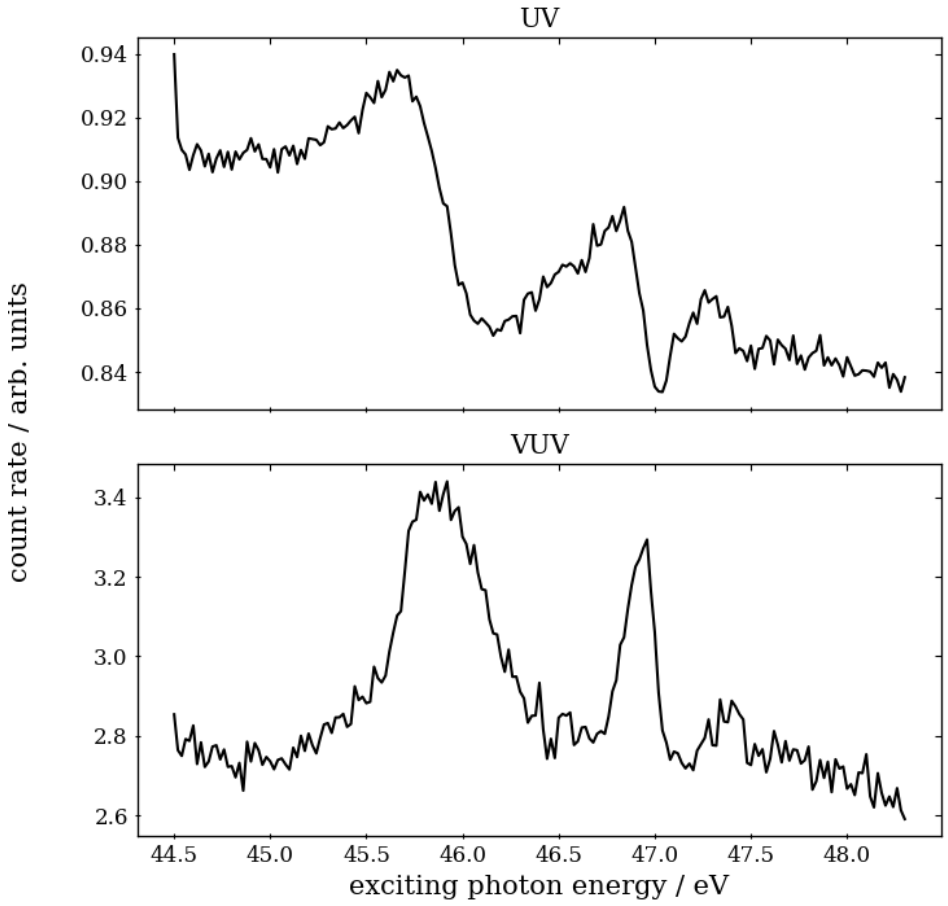

Figure A.2: Recorded fluorescence data in the UV (upper panel) and VUV (lower panel) regions. The x axis shows the exciting-photon energy around the $2s \rightarrow np$ resonances of neon. The y axis shows the respective detector counts normalized to the synchrotron's mirror current.

A.0.2 Slit Current

The following figure A.3 shows the slit current measured and representing atomic neon Auger electron features. Four of these features were numbered $(I - IV)$ and fitted with Fano shapes.

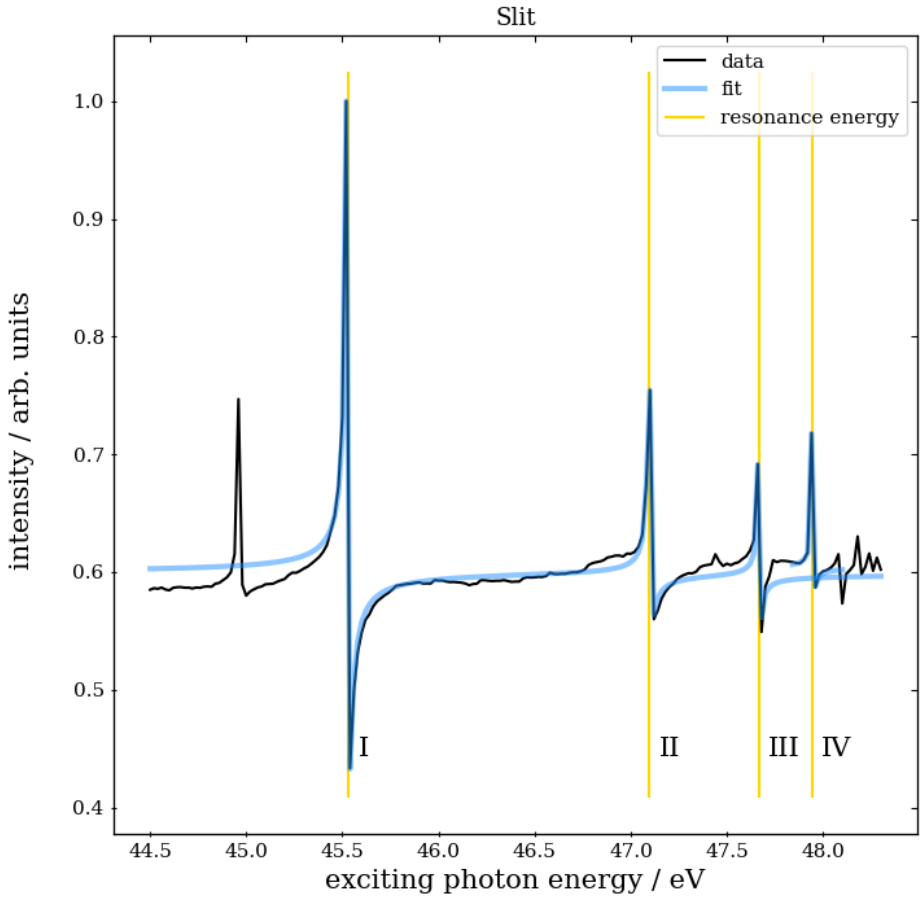

Figure A.3: Slit current displaying Fano resonances due to the atomic neon auger processes happening (black line). The fano features were multifitted with four resonances (blue curves, numbered $I-IV$). The yellow lines display the resulting position of the resonances.

The four fitted peaks included too many parameters for a quick fit. For this reason, the first three peaks were fitted by a sum of Fano' peaks just like in equations (3.3) and (3.4). The peak number IV was fitted with a single Fano peak shape and an offset. This method produces a discontinuity between peak III and IV, which is not further important for the consideration of the

resonance positions. The resonance frequencies obtained by the fit are

$$\begin{aligned} E_{r,I} &= (45.531 \pm 0.008)\,\mathrm{eV} \\ E_{r,II} &= (47.097 \pm 0.006)\,\mathrm{eV} \\ E_{r,III} &= (47.7 \pm 0.5)\,\mathrm{eV} \\ E_{r,IV} &= (47.94 \pm 0.08)\,\mathrm{eV}\,. \end{aligned}$$

Comparing these to the literature ([33]) values for the energy $E_{r,n,atom}$ of electronic resonant transitions $2s \rightarrow np$ with $n = 3, 4, 5, 6$ in atomic neon

$$\begin{aligned} E_{r,3,atom} &= 45.55\,\mathrm{eV} \\ E_{r,4,atom} &= 47.12\,\mathrm{eV} \\ E_{r,5,atom} &= 47.69\,\mathrm{eV} \\ E_{r,6,atom} &= 47.97\,\mathrm{eV}\,, \end{aligned} \tag{A.1}$$

one can quickly see that the values correspond very nicely to the determined resonance frequencies of the Fano shaped features. This is evidence for a correct energy calibration of the beam line.

A.0.3 Calibration

Figure A.4 shows the consecutive steps of the calibration graphically using gaseous nein. The magnetic bottle voltages during the presented calibration measurement were the same (4/4/2.1/0.1 V) as in the resonant excitation energy measurement presented in figure 3.4. Figure A.4a is a presentation of calibration data. For each exciting energies E_{ex} within the scan an electron spectrum was recorded (shown by the coloured lines). The energy was scaned in half eV-steps over the interval $E_{ex} \in [22, 28]$eV and in whole eV-steps from $E_{ex} = 28\,\mathrm{eV}$ to $E_{ex} = 46\,\mathrm{eV}$. The two bunches are observed separately (upper panel: bunch 1; lower panel: bunch 2). The position of the $2p$ photoelectron in each spectrum is calculated, which is fairly simply, since the peak is expected to be the most prominent feature.

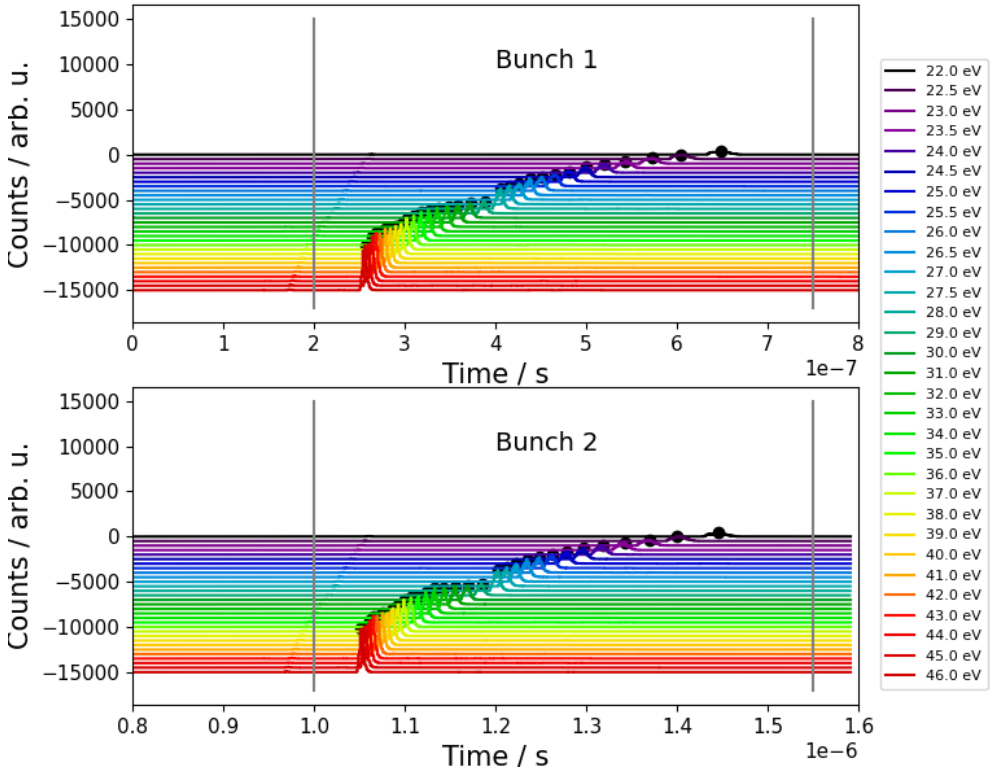

(a) photo electron peak tof

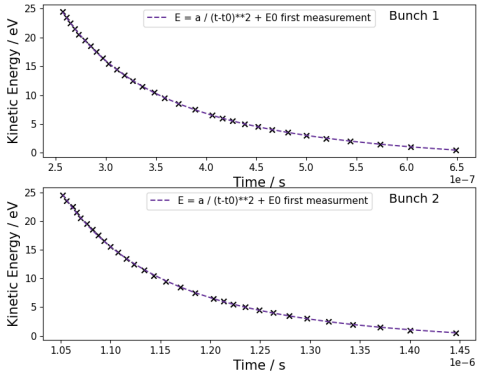

(b) excitation energy vs electron tof

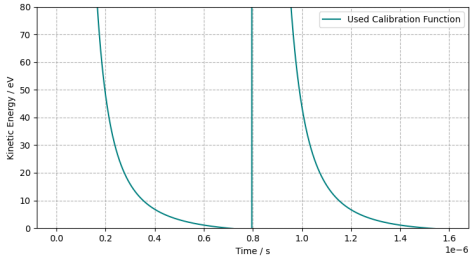

(c) final function

Figure A.4: Calibration broken down into three steps. (a) determination of $2p$ photo electron peak depending on exciting photon energy for each bunch. (b) Fitting of the photoelectron ToF vs exciting energy diagramm. (c) Resulting calibration function.

The next step, shown in A.4b, is to find the calibration function by determining the photo electon's tof dependency on the exciting photon energy. Both values should be related by the fundamental kinetic energy expression $E_{kin} = \frac{1}{2}mv^2$. By introducing the length L of the drift tube and the measured time of flight $t_{tof} = t$ of the electrons this expression becomes

$$E_{kin} = \frac{1}{2}m\left(\frac{L}{t}\right)^2 . \tag{A.2}$$

A calibration function $E_{1/2}$ for each bunch 1 and 2 based on the relation above is approximated as

$$E_{1/2} = \frac{a_{1/2}}{(t - t_{0,1/2})^2} + E_{0,1/2}\,, \tag{A.3}$$

where $a_{1/2}$, $T_{0,1/2}$ and $E_{0,1/2}$ are fitting parameters, while t is the measured tof. The fit can be seen in the figure A.4b for each bunch separately and the final calibration function E is a combination of both calibration functions E_1 and E_2

$$E = \begin{cases} E_1, & \text{if } t < t_B \\ E_2, & \text{if } t \geq t_B \end{cases} . \tag{A.4}$$

The final calibration function is shown in A.4c. The function yields unreasonably high kinetic energies for $t < 200\,\text{ns}$ and $800\,\text{ns} < t < 1000\,\text{ns}$. This collides with the fundamental concept of energy conservation, since the emitted electrons are not able to gain more energy than was introduced into the system by the synchrotron radiation. This divergence can be explained by the narrow width of time of flights that was covered by the $2p$ photo electron signal in the calibration scan (area within the gray lines in figure A.4a). This could be improved using a bigger scanning range or secondary features that cover different times of flight regimes. For the calibration in this case, the calibrated data exceeding the excitation energy were disregarded.
The raw electron tof data point from measurements involving the same magnetic bottle parameter setting are converted into kinetic energies of the electron using the calibration function. The same is done analogously for other measurements with different magnetic bottle settings.
The following figure A.5 show the calibrated electron-photon coincidence maps.

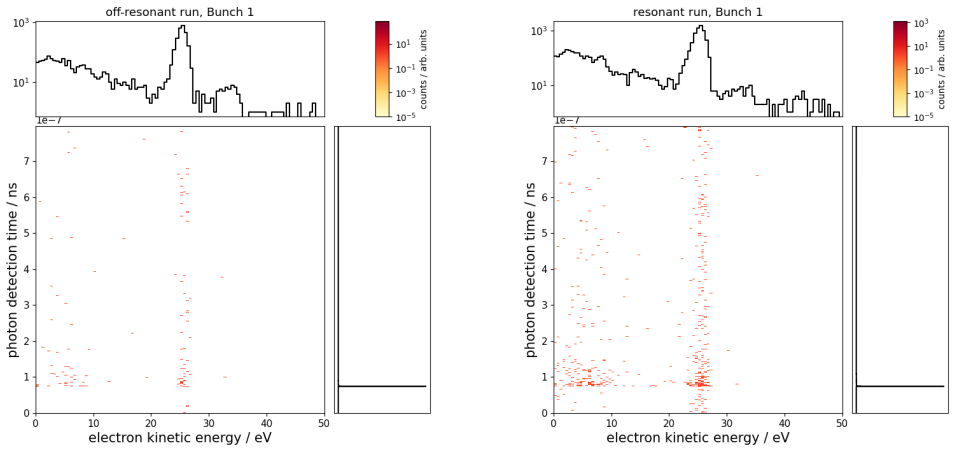

(a) off-resonant excitation (b) resonant excitation

Figure A.5: Calibrated coincidence maps for the first bunch. The different maps show different excitation energies of the synchrotron beam. One energy lying on the $2s \rightarrow 4p$ resonance and one slightly off.

A.0.4 Energy Scan

Figure A.6 shows the electron spectrum recorded for each energy step during the scan in a colour map. The energy was scanned from 46.8 eV up to 47.2 eV in 0.01 eV-steps. The electron spectra were binned with a bin width of $w_b = 0.1$ eV.

Despite the low resolution, the total electron signal for each exciting energy step (right panel) shows the same fano-like peak shape around the $2s \rightarrow 4p$ resonance as was discussed in the fluorescence section of the analysis chapter 3.1.

The two features mentioned in the coincidence chapter 3.2 are marked by dashed lines in the upper panel, which is the integrated electron spectrum over all exciting energies in the scan. The broad feature named rICD was assigned to the electrons produced by the rICD and the second peak by $2p$ photo electrons that were scattered within the cluster by literature [16]. In the colour map the dependence of the scatter $2p$ peak on the exciting photon energy is present. The peak and the minimum between the peaks are shifting to higher kinetic energies with higher exciting energies. The two dashed lines

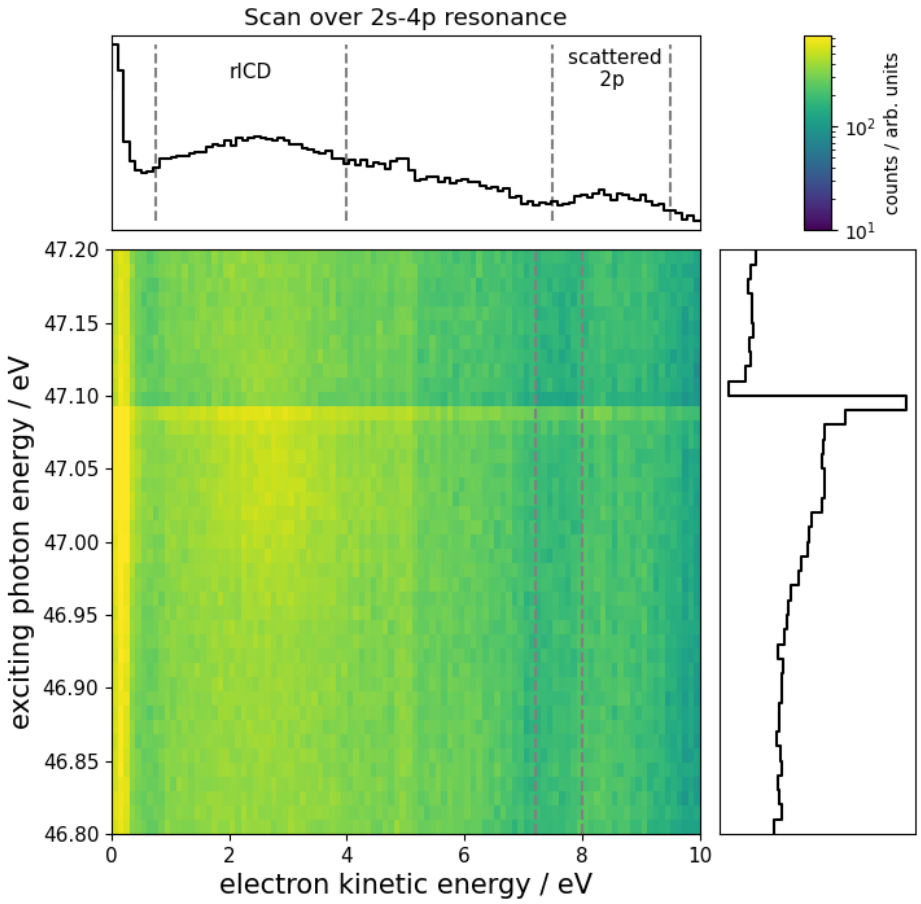

Figure A.6: Colour map of electron kinetic energies in dependency on the exciting photon energy.

in the map are suppose to guide the eye as vertical lines in order to visualize this phenomenon in the data.
Lastly, the rICD peak seems to have a maximum in the vicinity of the resonance energy when looking at the intensity of the colour map. This corresponds with expectations about this interatomic process.

A.0.5 Cut-Off

In order to determine the photon detection time cut-off, the coincidence maps are enhanced around the strong photo lines seen in figure 3.3. The cut-off is chosen such that most of the line is not included in further data analysis, but keeping minimal loss of the total signal to not weaken the resolution.

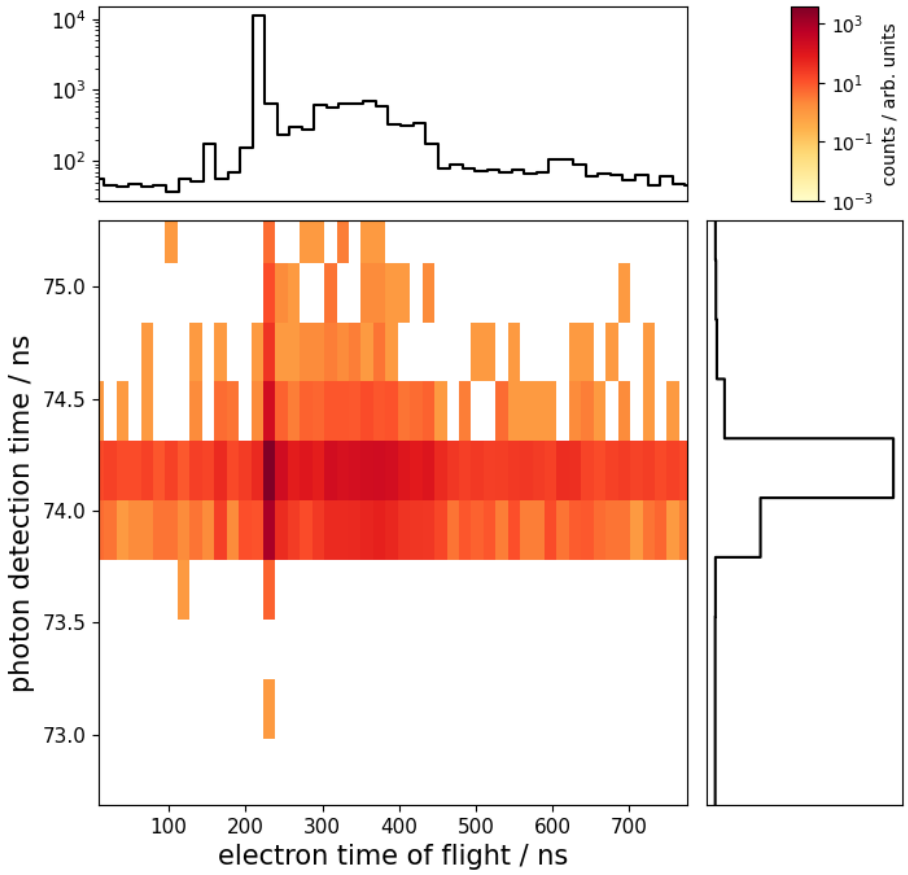

Figure A.7: Zoom into the coincidence map of electron-photon events created after off-resonant neon cluster excitation.

Bibliography

[1] Amos De Shalit. *The feynman lectures on physics: vol. III, by Richard P. Feynman, Robert B. Leighton and Matthew Sands. vp diagrams, 8built14× 11 X 11 in. Reading, Mass. Addison-Wesley Publ. Co., 1965. Price, $6.75*. Pergamon, 1967.

[2] Hans C. Wolf Hermann Haken. *Molekuelphysik und Quantenchemie*. 4., völlig neu bearb. u. erw. Aufl. Springer-Lehrbuch. Springer, 2002. ISBN: 9783540435518,3540435514,3540303146.

[3] Andrei Tokmakoff. *Book: Time Dependent Quantum Mechanics and Spectroscopy (Tokmakoff)*. [Online; accessed 2021-04-01]. Dec. 12, 2020. URL: https://chem.libretexts.org/@go/page/107215.

[4] Gilbert Grynberg Claude Cohen-Tannoudji Jacques Dupont-Roc. *Photons and atoms: Introduction to quantum electrodynamics*. Wiley Professional. Wiley-VCH, 1997.

[5] John Weiner and P-T Ho. *Light-matter interaction: fundamentals and applications*. Vol. 1. John Wiley and Sons, 2008.

[6] Professor Bipin K. Agarwal Ph. D. (auth.) *X-Ray Spectroscopy: An Introduction*. 2nd ed. Springer Series in Optical Sciences 15. Springer-Verlag Berlin Heidelberg, 1991. ISBN: 978-3-540-50719-2,978-3-540-38668-1.

[7] Elisabeth Heinrich-Josties, Stefan Pabst, and Robin Santra. "Controlling the $2p$ hole alignment in neon via the $2s$-$3p$ Fano resonance". In: *Phys. Rev. A* 89 (4 Apr. 2014), p. 043415. DOI: 10.1103/PhysRevA.89.043415. URL: https://link.aps.org/doi/10.1103/PhysRevA.89.043415.

[8] U. Fano. "Effects of Configuration Interaction on Intensities and Phase Shifts". In: *Phys. Rev.* 124 (6 Dec. 1961), pp. 1866–1878. DOI: 10.1103/PhysRev.124.1866. URL: https://link.aps.org/doi/10.1103/PhysRev.124.1866.

[9] LS Cederbaum, J Zobeley, and F Tarantelli. "Giant intermolecular decay and fragmentation of clusters". In: *Physical review letters* 79.24 (1997), p. 4778.

[10] Andreas Hans. "Fluoreszenzspektroskopie an Clustern & Flüssigkeiten-Untersuchung interatomarer und intermolekularer Prozesse in dichten Medien". PhD thesis. 2018.

[11] Simon Marburger et al. "Experimental evidence for interatomic Coulombic decay in Ne clusters". In: *Physical review letters* 90.20 (2003), p. 203401.

[12] T. Jahnke et al. "Experimental Observation of Interatomic Coulombic Decay in Neon Dimers". In: *Phys. Rev. Lett.* 93 (16 Oct. 2004), p. 163401. DOI: 10.1103/PhysRevLett.93.163401. URL: https://link.aps.org/doi/10.1103/PhysRevLett.93.163401.

[13] T Ouchi et al. "Three-electron interatomic coulombic decay from the inner-valence double-vacancy states in NeAr". In: *Physical review letters* 107.5 (2011), p. 053401.

[14] Philipp HP Harbach et al. "Intermolecular Coulombic Decay in Biology: The Initial Electron Detachment from FADH–in DNA Photolyases". In: *The journal of physical chemistry letters* 4.6 (2013), pp. 943–949.

[15] Till Jahnke et al. "Interatomic and Intermolecular Coulombic Decay". In: *Chemical Reviews* 120.20 (2020), pp. 11295–11369.

[16] S Barth et al. "Observation of resonant interatomic coulombic decay in Ne clusters". In: *J Chem Phys* 122.24 (June 2005), p. 241102. DOI: {10.1063/1.1937395}.

[17] V Averbukh et al. "Interatomic electronic decay processes in singly and multiply ionized clusters". In: *Journal of Electron Spectroscopy and Related Phenomena* 183.1-3 (2011), pp. 36–47.

[18] T Jahnke et al. "Experimental separation of virtual photon exchange and electron transfer in interatomic Coulombic decay of neon dimers". In: *Physical review letters* 99.15 (2007), p. 153401.

[19] Andreas Hans et al. "Fluorescence cascades evoked by resonant interatomic Coulombic decay of inner-valence excited neon clusters". In: *Chemical Physics* 482 (2017), pp. 165–168.

[20] Andreas Hans et al. "Direct evidence for radiative charge transfer after inner-shell excitation and ionization of large clusters". In: *New Journal of Physics* 20.1 (2018), p. 012001.

[21] Gregor Schiwietz, Martin Beye, and Torsten Kachel. "UE112_PGM-1: An open-port low-energy beamline at the BESSY II undulator UE112". In: *Journal of large-scale research facilities JLSRF* 1 (2015), p. 33.

[22] Albert Hofmann. *The physics of synchrotron radiation*. Vol. 20. Cambridge University Press, 2004.

[23] Andreas Hans et al. "Extreme Ultraviolet to Visible Dispersed Single Photon Detection for Highly Sensitive Sensing of Fundamental Processes in Diverse Samples". In: *Materials* 11.6 (2018). ISSN: 1996-1944. DOI: 10.3390/ma11060869. URL: https://www.mdpi.com/1996-1944/11/6/869.

[24] Joseph Ladislas Wiza et al. "Microchannel plate detectors". In: *Nucl. Instrum. Methods* 162.1-3 (1979), pp. 587–601.

[25] A Hans et al. "Setup for multicoincidence experiments of photons in the extreme ultraviolet to visible spectral range and charged particles—The solid angle maximization approach". In: *Review of Scientific Instruments* 90.9 (2019), p. 093104.

[26] Hellmut Haberland. *Clusters of atoms and molecules: theory, experiment, and clusters of atoms*. Vol. 52. Springer Science & Business Media, 2013.

[27] H Schmoranzer et al. "Photon-induced fluorescence spectroscopy (PIFS)". In: *Nuclear Instruments and Methods in Physics Research Section A: Accelerators, Spectrometers, Detectors and Associated Equipment* 467 (2001), pp. 1526–1528.

[28] André Knie et al. "Detecting ultrafast interatomic electronic processes in media by fluorescence". In: *New Journal of Physics* 16.10 (2014), p. 102002.

[29] Andreas Hans et al. "Determination of absolute cross sections for cluster specific decays". In: *Journal of Physics B: Atomic, Molecular and Optical Physics* 49.10 (2016), p. 105101.

[30] Andreas Hans et al. “Electronic Decay of Singly Charged Ground-State Ions by Charge Transfer via van der Waals Bonds”. In: *Physical Review Letters* 123.21 (2019), p. 213001.

[31] A Kivimäki et al. “Dissociative photoionization of the NO molecule studied by photoelectron–photon coincidence technique”. In: *Journal of Electron Spectroscopy and Related Phenomena* 182.1-2 (2010), pp. 63–69.

[32] Melanie Mucke et al. “Performance of a short “magnetic bottle” electron spectrometer”. In: *Review of Scientific Instruments* 83.6 (2012), p. 063106.

[33] *National Institute of Standards and Technology Atomic Spectra Database Lines Data: Neon*. 2021.

[34] Roman Flesch et al. “2s-Excitation and Photoionization of Neon Clusters”. In: *Zeitschrift für Physikalische Chemie* 228.4-5 (2014), pp. 387–403.